Int J Fract
https://doi.org/10.1007/s10704-024-00836-w

RESEARCH

Heterogeneous fracture toughness of human cortical bone tissue

Maxime Levy · Zohar Yosibash

Received: 30 June 2024 / Accepted: 29 December 2024

Abstract CT-based finite element analysis (FEA) of human bones helps estimate fracture risk in clinical practice by linking bone ash density (ρ_{ash}) to mechanical parameters. However, phase field models for fracture prediction require the heterogeneous fracture toughness G_{Ic}, which can be derived from the critical stress intensity factor K_{Ic}, determined through various experimental methods. Due to a lack of standards for determining cortical bone's K_{Ic}, an experimental campaign is presented using 53 cortical specimens from two fresh frozen femurs to investigate whether a correlation exists between K_{Ic} and ρ_{ash}. We investigated various experimental techniques for correlating K_{Ic} with ρ_{ash}. We conducted FEAs employing the phase field method (PFM) to determine the most suitable correlation among the five possible ones stemming from the experimental methods. The ASTM standard using displacement at force application point was found to be the recommended experimental method for the estimation of K_{Ic} perpendicular to osteons' direction

$$K_{Ic}[MPa\sqrt{m}]=1.89\,(\rho_{ash}[gr/cc])^{1.88}\quad R^2=0.5374.$$

The corresponding statistical critical energy release rate bounds were determined:

$$G_{Ic}[N/m] = 321.94(\rho_{ash}[gr/cc])^{1.69} \times exp(\pm 2SD),$$

with a standard deviation $SD = 0.30$ representing a 95.4% confidence interval. The average G_{Ic} resulted in good correlations between the predicted fracture force by PFM-FEA of four representative specimens and experimental fracture forces. The proposed correlations will be used in CT-based PFM FEA to estimate the risk of hip and humeral fractures.

Keywords Fracture toughness · Cortical bone · Heterogeneous material · Phase field model

Notations

FPZ	Fracture process zone
FM	Fracture mechanics
L-C	Longitudinal-circumferential
L-R	Longitudinal-radial
ASTM	American Society for Testing and Materials
LLD	Load line displacement
COD	Crack opening displacement
RILEM	International union of laboratories and experts in construction materials, systems and structures (from the name in French)
3PB	Three-point bending
SEN(B)	Single-edge notched beam
DIC	Digital image correlation
QCT	Quantitative computed tomography
GV	Gray value
HA	Hydroxyapatite
HU	Hounsfield units

M. Levy · Z. Yosibash (✉)
School of Mechanical Engineering, The Iby and Aladar Fleischman Faculty of Engineering, Tel-Aviv University, HaLevanon st, Ramat Aviv 69978, Israel
e-mail: yosibash@tauex.tau.ac.il

Published online: 24 January 2025

CTFEA	Computed tomography based finite element analysis
PFM	Phase field model
SNES	Scalable nonlinear equations solvers
TAO	Toolkit for advanced optimization

Nomenclature

K_{Ic}	Critical stress-intensity factor
G_{Ic}	Critical energy-release rate
E	Young's modulus
λ And μ	Lamé parameters
ν	Poisson's ratio
J_{Ic}	Critical J-integral value
ρ_{ash}	Bone ash density
$\rho_{K_2HPO_4}$	Phantom's density (qCT)
BV/TV	Bone volume/total volume
L	Specimen's length
W	Specimen's width
B	Specimen's thickness
a_0	Specimen's notch length
ω	Specimen's notch angle
ρ	Specimen's notch tip radius
U_t	Applied displacement
P/v	Force/displacement
P_Q^v And P_Q^{COD}	provisional fracture force calculated from LLD and COD
C_i And C_u	initial and ultimate compliance
R^2	Coefficient of determination
Π	Energy functional
$\underline{\underline{\varepsilon}}$	Linear strain tensor
$\underline{\underline{\sigma}}^0$ And $\underline{\underline{\sigma}}$	Cauchy's stress tensor associated with undamaged and damaged state
$\underline{u}$	Displacement field
α	Damage field
ℓ_0	Internal length
Ω	Specimen's 2D domain
k_{res}	Residual stiffness
h_{min} And h_{max}	minimum and maximum element size
h_{top}	Element size where the displacement is applied
y_0	Displacement application length
Δ_t	Displacement load increment
P^{FE} And P^{EXP}	force determined from FEA and experimental results

1 Introduction

Analysis of computer tomography scans (CT scans) enables the creation of patient-specific bone geometry, and by correlating Young's modulus with CT-derived density values, it becomes possible to map the distribution of material properties within the bone structure (Keyak and Falkinstein 2003). These techniques, utilized in CT-based finite element analyses (CTFEA), may predict the mechanical behavior of healthy and diseased femurs (Yosibash et al. 2007; Schileo et al. 2008a; Trabelsi et al. 2011; Yosibash et al. 2014). However, while CTFEA excels in predicting mechanical responses, it struggles with accurately determining the instance of fracture initiation based on a threshold principal strain (Schileo et al. 2008; Yosibash et al. 2010).

Recent advancements in fracture initiation theories, such as the phase field model (PFM), have attracted significant interest for their potential to more accurately predict bone failure load at the organ level. Initial trials using PFMs for fracture prediction have shown promise (Shen et al. 2019; Hug et al. 2022; Preve et al. 2024). Nonetheless, a critical challenge still lies in determining the fracture toughness (K_{Ic} or G_{Ic}) at the macro-scale, which varies within bone and is presumed to be correlated with bone ash density, yet its distribution remains unknown. Additionally, there are no established standards for bone fracture testing to measure these properties.

Given the relevance of bone fractures under physiological loading, particularly involving transverse crack propagation, our focus is on the L-R direction (Fig. 1).

At the micro-scale cortical bone may exhibit minor non-linearities as a result of toughening mechanisms such as crack deflection, uncracked-ligament bridging and micro-cracks (Zioupos and Currey 1998; Ritchie et al. 2009; Zimmermann et al. 2010), but at the organ level in long bones such as femurs, a brittle-like fracture occurs (Juszczyk et al. 2011). Thus, the relation $G_{Ic} = K_{Ic}^2(1-\nu^2)/E$ is assumed to be valid (here ν is the Poisson ratio). To measure the fracture toughness at the macro-level experimental protocols have to be applied, but unfortunately, none exist for bones.

Several experimental techniques exist for measuring K_{Ic}, such as those outlined in ASTM standards (ASTM-E399 1990; ASTM-E1820 2011), employing the P_Q load (see Fig. 2a). However, as these standards are not tailored for bone, an alternative approach introduced in Zioupos and Currey (1998) substitutes

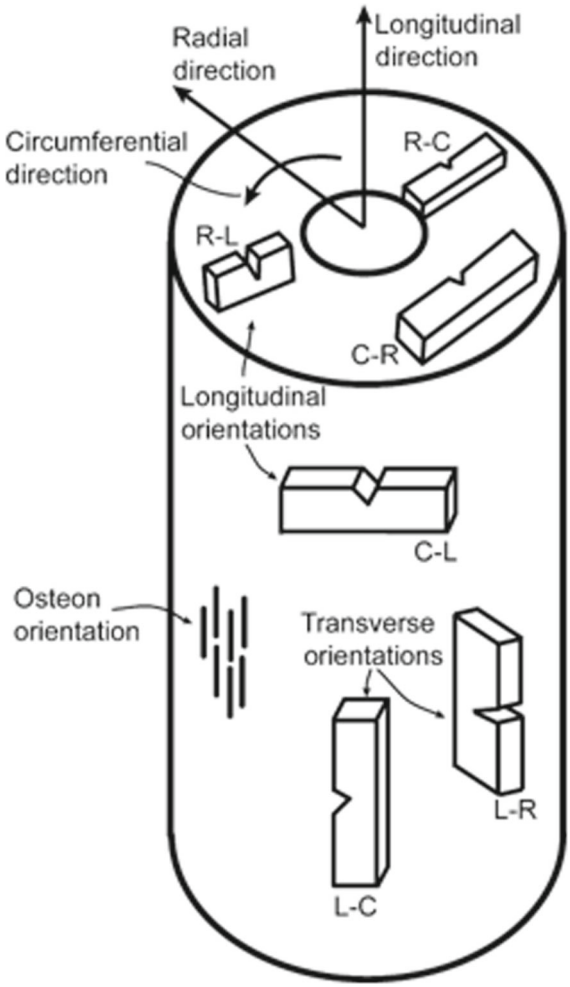

Fig. 1 Specimen types (Ritchie et al. 2005)

the maximum force P_{max}, argued to better mimic crack growth conditions. Another method involves considering minor non-linearities as plastic phenomena, constructing a *J-R curve* to derive J_{Ic} (see Fig. 2b), and then determining K_{Ic} value following (ASTM-E1820 2011), as demonstrated in Ritchie et al. (2005), Koester et al. (2008), Granke et al. (2015).

Alternatively, a fracture process zone (FPZ) approach incorporating micro-cracks, used for concrete testing applying RILEM standards (RILEM-TC-089-FMT 1991; Carpinteri et al. 2017) (see Fig. 2c) has been proposed to assess bone K_{Ic}. The application of these standards to notched bone specimens has yielded K_{Ic} values, regardless of bone density, as summarized in Table 1. Specimens were extracted from the mid-shaft of human long bones, except in Carpinteri et al. (2017), where bovine femurs were utilized (therefore, not presented). Given the significant variability in K_{Ic} values obtained through the *J-R curve* method and considering bone tissue's quasi-brittle nature (Zioupos and Currey 1998; Granke et al. 2016), this particular method is omitted from the present study.

To the best of our knowledge, G_{Ic} in transverse orientation, required for a PFM analysis, has only been determined by a graphical method considering the critical J-integral value, denoted $J_{ini} = 900 - 1350\,\mathrm{N/m}$ (Zioupos and Currey 1998). This value represents the energy necessary for crack growth without assuming linearity at the notch. No correlations are available between a CT-based bone ash density ρ_{ash} and K_{Ic} or G_{Ic}. Establishing experimental relationship $G_{Ic}(\rho_{ash})$ is mandatory for bone fracture prediction using CT scans and PFM.

The closest-related former publications (Yeni et al. 1998; Yeni and Norman 2000b) investigated the correlation between G_{Ic} and wet and dry apparent density, and the apparent and real percentage of mineral, organic, and water contents. Compact-tension specimens were extracted from human femurs, precracked longitudinally, and tested to determine G_{Ic} using the compliance method. Unfortunately, correlations between qCT-based bone density and K_{Ic} or G_{Ic} are not provided in the literature for cortical bone and transverse crack propagation.

To fill this gap, an experimental campaign is presented by which three-point-bending (3PB) notched human cortical bone specimens are used to determine $K_{Ic}(\rho_{ash})$ relationship in the transverse direction. The ASTM and RILEM standards are followed in our experiments.

We used two fresh frozen femurs and performed qCT scans to obtain the ρ_{ash} distribution. We sliced the femurs into 3PB specimens and inserted V-notches, ensuring that the ρ_{ash} is known at the V-notch tip. We performed micro-CT scans on each 3PB specimen to determine whether the density is constant along the V-notch edge. This step helped us discard specimens that had an inclined edge or a large distribution of densities along the edge. 3PB tests with Digital Image Correlation (DIC) were thereafter conducted to measure the Load Line Displacement (LLD), denoted as v, and the Crack Opening Displacement (COD). Using ASTM and RILEM standards, K_{Ic} for each specimen was determined, based on which we established the relationship $K_{Ic}(\rho_{ash})$. $K_{Ic}(\rho_{ash})$ and $E(\rho_{ash})$ were

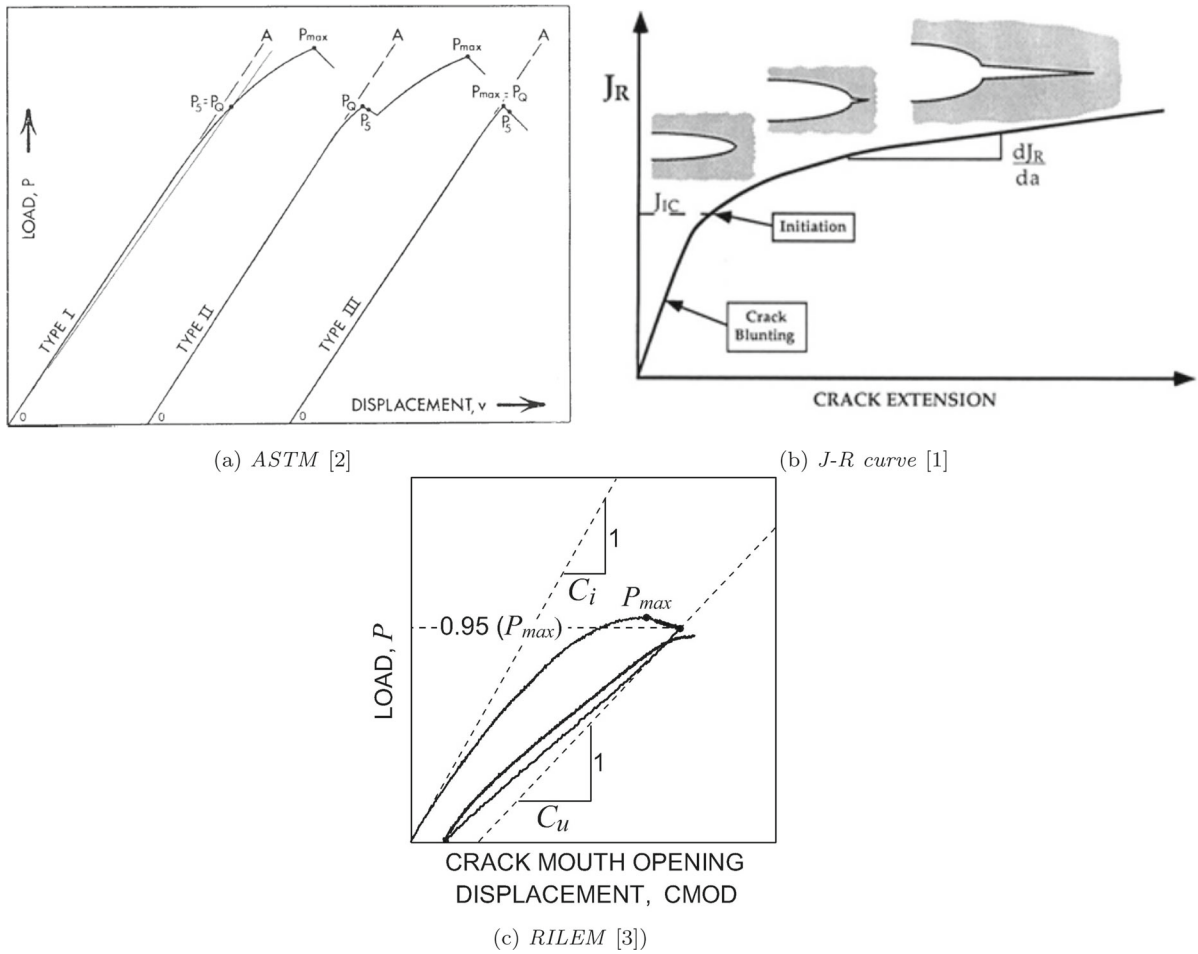

(a) *ASTM* [2] (b) *J-R curve* [1]

(c) *RILEM* [3])

Fig. 2 Typical curves of the three methods for K_{Ic} determination in bone specimens

Table 1 Past experimental results using 3PB or compact tension specimens. Specimens were taken from human cortical femurs (Fem) or humeri (Hum). N/A - not available

Reference	Anatomical site	# of Spe.	Direction.	Method	K_{Ic} $MPa\sqrt{m}$
Zioupos and Currey (1998)	Fem	30	L-C	*ASTM*	$5-7$
Wang et al. (2002)	Fem	30	N/A	*ASTM*	5.23 ± 1.15
Nalla et al. (2005)	Hum	3	L-C	*ASTM*	5.3 ± 0.4
Nalla et al. (2005)	Hum	3	C-R	*ASTM*	2.2 ± 0.2
Koester et al. (2008)[1]	Hum	17	L-C	*J-R curve*	1
Granke et al. (2015)	Fem	62	N/A	*J-R curve*	$5-15$

[1] Short pre-crack

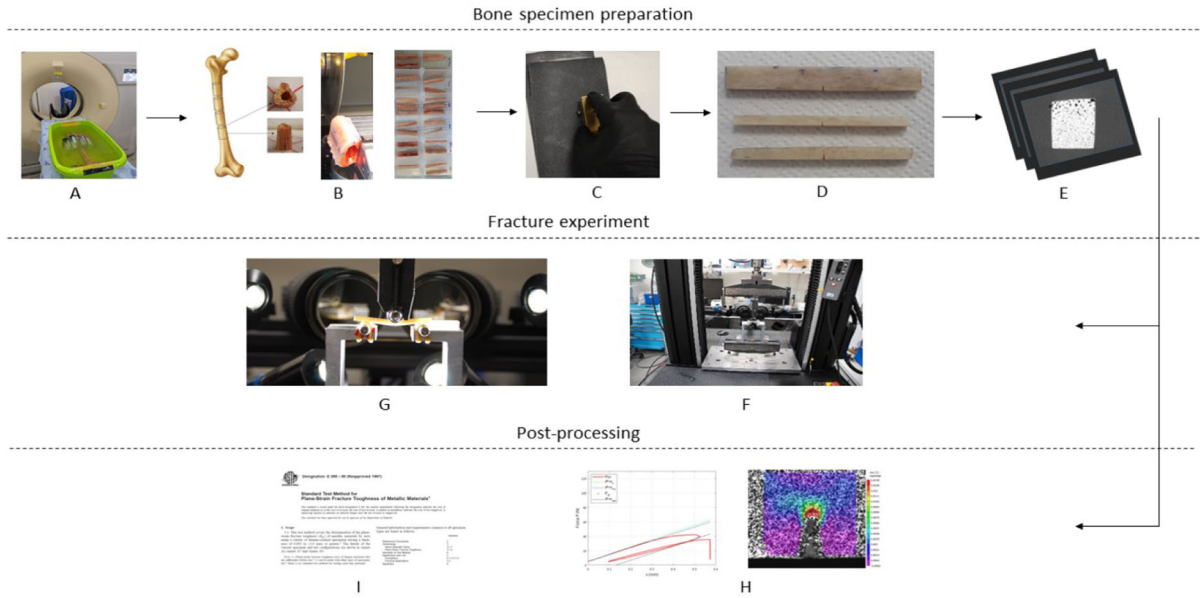

Fig. 3 Experimental flowchart - determine $K_{Ic}(\rho_{ash})$ **A** Clinical CT scan of a human femur. **B** Cutting into specimens. **C** Specimen polishing. **D** Notching. **E** Micro-CT. **F** 3PB setup. **G** DIC setup. **H** Illustration test and DIC results. I ASTM & RILEM standards (E399-90, TC-089-FMT)

Table 2 QCT-scan acquisition details

Parameters	Bone 1#	Bone 2#
In-plane resolution (mm)	0.3	0.21
Slice thickness (mm)	0.67	0.4

used to compute $G_{Ic}(\rho_{ash})$. Finally, to identify the best relationship, four representative test cases were randomly selected and PFM-based Finite Element Analyses (FEA) were performed.

This detailed process ensures that a reliable correlation between bone density and fracture toughness is found, which is crucial for predicting bone fractures using CT scans and PFM methodologies.

2 Materials and methods

Fifty-eight specimens were extracted from two fresh-frozen femoral bones following qCT of the whole bones. The specimens were polished and notched at their center, thereafter re-scanned by micro-CT. The specimens were then painted to allow digital image correlation (DIC) measurements while they were fractured in a 3PB setup. The experimental flowchart, from specimen preparation to post-processing of the fracture tests, is illustrated in Fig. 3.

2.1 Estimation of ρ_{ash}

Two femurs from 77-year-old donors, a female (bone #1, weight: 112 kg) and a male (bone #2, weight: 42 kg), with no history of skeletal diseases, were CT scanned immersed in water with K_2HPO_4 phantoms. The clinical qCT scan was performed by a Philips iCT 256 scanner(Eindhoven, Netherlands), without overlap, at 120 kVp and 300 mAs tube current as documented in Table 2.

Metal markers (blue circles in Fig. 4a) were attached to the shaft so that all specimens cut from the bone could be identified so to determine their spatial density distribution. An top view of the qCT scan with calibration phantoms and density to HU correlation are shown in Fig. 4.

The ash density ρ_{ash} is associated with HUs by Schileo et al. (2008a).

$$\rho_{ash} = 0.877 \times 1.15\rho_{K_2HPO_4} + 0.08 \quad [gr/cm^3]$$
$$R^2 = 0.997 \tag{1}$$

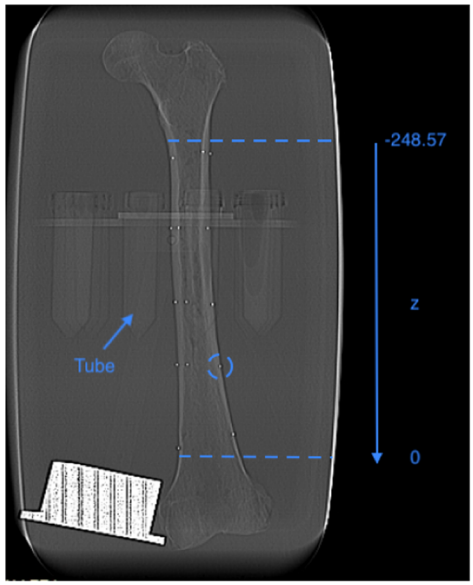

(a) Top view

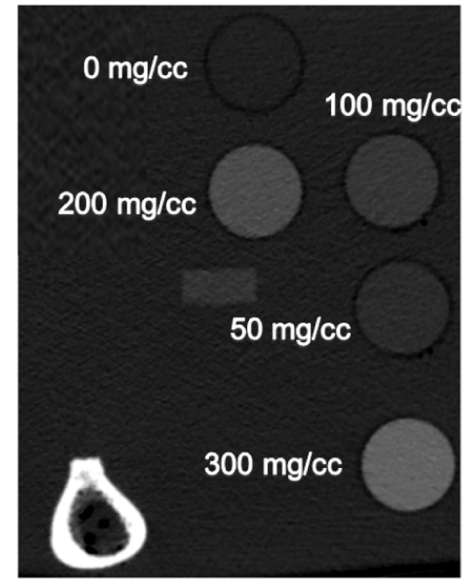

(b) Phantoms (slice)

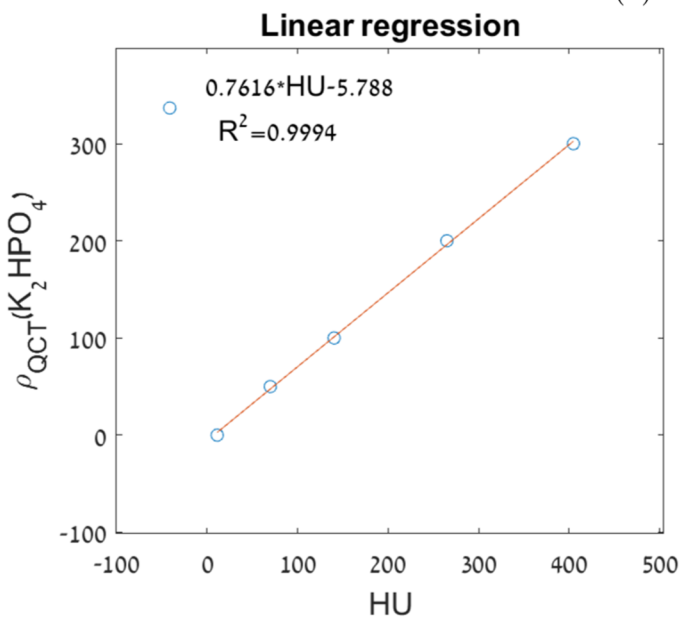

(c) Calibration curve

Fig. 4 Clinical qCT indicates the segmented part (delimited by dotted blue line), the z axis, the metal markers (surrounded by blue circle) and the phantom tubes

Equation (1) provides the distribution ρ_{ash} within the 3PB extracted specimens, and especially at the notch front, as illustrated in Fig. 5. Three average densities were calculated for three cuboids of approximate size $0.9 \times 0.9 \times 2.1$ mm^3 located along the notch front. The density value ρ_{ash} was taken as the average of the density values.

By extracting L-R specimens (see Fig. 1), ρ_{ash} varies in the radial direction (the crack propagation direction) while ρ_{ash} along the notch front was inspected to ensure it did not vary by more than 10% as observed in Fig. 5.

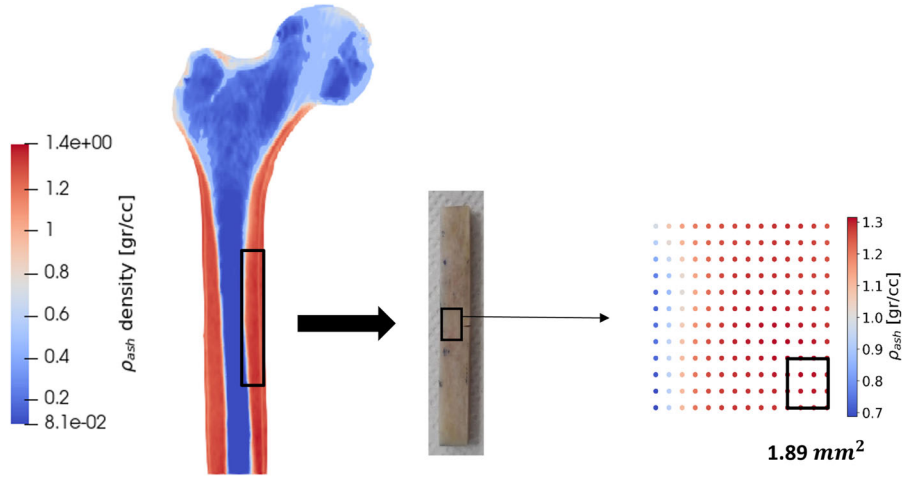

Fig. 5 Estimation of ρ_{ash} in the vicinity of the notch tips in the 3PB specimens

The density is highest at the outer surface of the bone and decreases toward the inner surface of the bone. The estimated ρ_{ash} was validated by the micro-CT results in Sect. 2.3.

2.2 Specimens preparation

The 58 single-edge notched beam (SEN(B)) specimens, approximately 50 mm long, were cut from the femur shaft along L-R orientations using a Brilliant 220 cutting machine and a Proxxon 27006 disk saw (see Fig. 6). The width and thickness of the specimens ranged between 3.15−5.22 mm and 2.54−3.86 mm, respectively. The specimens were polished using 150 and 240 grit sandpapers to obtain smooth surfaces for 3PB experiments.

Notches were inserted by an IsoMet Low Speed precision cutter and a GSP disk saw (see Fig. 7). The notches had an angle $\omega = 10°$ and a tip radius of 40–50 μm with depth ratio a_0/W ranged between 0.18−0.40. The dimensions W, B were measured using a caliper (0.01 mm resolution) and a_0 using micro-CT data with a resolution of 40 μm. The notch depth of a dozen of specimens was also measured with an optical microscope to validate the μCT-based measurements. The specimen's dimensions are reported in Table 3.

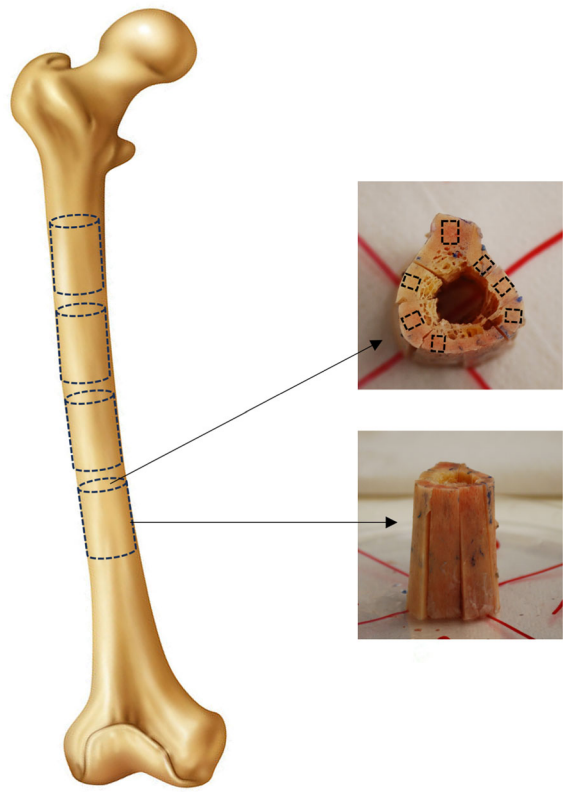

Fig. 6 Representation of the femur, the 4 cylinders cut with Brilliant machine and the specimens obtained after polishing (dashed lines)

2.3 Micro-CT scans

The notched specimens were micro-CT scanned using a μCT Nikon XT H 225 ST scanner. The scans were used to extract specimens' microstructure and porosity in the area of the notch. Specimens were immersed in Ringer's solution and scanned at 180 kVp, voxel size of 40 μm^3 and Hydroxyapatite (HA) phantoms (see

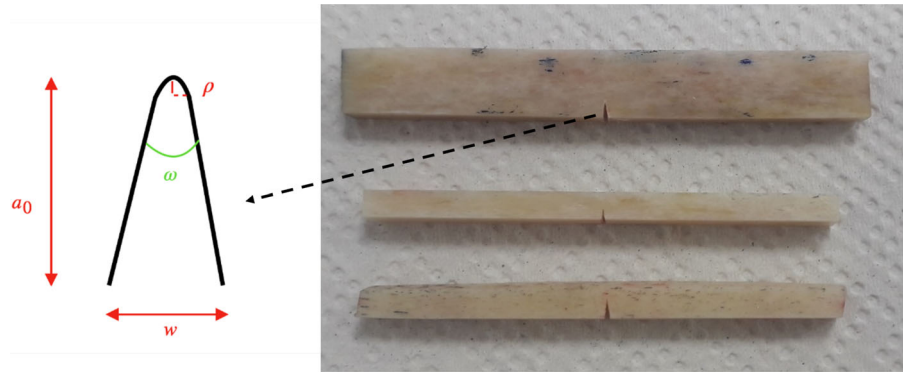

Fig. 7 Notched specimens and representation of notch geometry, $\omega = 10°$, $w = 0.3$ mm, $0.04 \le \rho \le 0.05$ mm and $0.81 \le a_0 \le 1.83$ mm

Fig. 8). For the segmentation of the bone tissue a global threshold HA was used, 1000 $HAmg/cc$ (Shim et al. 2022) and corresponding threshold gray value (GV) 53600-56500 GV.

One may use the porosity to validate the qCT-based density values especially regarding the specimens excluded due to high variability in density values along the notch front. We compared the 2D μCT-slice at the notch front with the corresponding ones obtained at the assumed slice in the clinical qCT-scan. A typical example is shown in Fig. 9.

We also calculated the *BoneVolume/TotalVolume* (BV/TV) for three cuboids of approximate size $0.9 \times 0.9 \times 2.1$ mm^3 located along the notch front. The averaged BV/TV was correlated with the qCT-based ρ_{ash} density in Fig. 10 and as expected ρ_{ash} increases as porosity decreases i.e BV/TV increases.

2.4 3PB experiments

3PB experiments were performed using an Instron 68TM-30 testing machine with a 25 kN load cell capacity. A loading rate of 1 mm/min was applied, and the force to load line displacement (LLD) curve was recorded. If a 5% decrease in force was measured after the peak force, the *RILEM* standards were applied, and the specimen was unloaded at a rate of 0.75 mm/min, then reloaded until fracture. A 20th-order one-dimensional median filter was applied to the measured data to obtain a smooth force-displacement curve. The force-displacement curves were used to determine the load P_Q (*ASTM* standards) and the loading and unloading compliance, C_i and C_u (*RILEM* standards).

Two displacement measurements were recorded during 3PB test: load line displacement (LLD denoted also by v) and crack opening displacement (COD). LLD is the crosshead displacement of the loading machine, while COD is the displacement between the two notch faces. COD is more sensitive and recommended in the standards but LLD was used in past experimental results probably due to technical difficulties of a clip gauge. To overcome the technical difficulties we performed DIC measurements to measure COD during the fracture test. We used Vic 3D software v 7.2.6 (Correlated Solutions Incorporated) to record the strains and COD via DIC technique.[1] Two cameras (5.0 Megapixel Digital Cameras USB-3, 30fps, Correlated solutions), two macro lenses (Tokina 100 mm 1:1) and 4 light spots were used for the DIC. Analog data from the Instron machine was synchronized with the DIC images using a data acquisition card (USB-6212 by National Instruments, Austin, USA). A typical 3PB experiment is shown in Fig. 11.

2.5 Quality control measures

We used micro-CT and DIC results to check for the presence of notch defects, resulting in the exclusion of 3 specimens (#12, #29 from bone #1 and #15 from bone #2). Two specimens (#23 from bone #1 and #22 from bone #2) were excluded because ρ_{ash} variations exceeded 10% along the V-notch front. Thus experimental correlations $K_{Ic}(\rho_{ash})$ and $G_{Ic}(\rho_{ash})$ were determined using 53 specimens, 21 from bone #1 and 32 from bone #2.

Among all possible relations $G_{Ic}(\rho_{ash})$ obtained by the various experimental techniques, the one that best

[1] Interrogation window size (subset in Vic 3D terminology) of 31 × 31 to 57 × 57 pixels with 75% overlap (8 to 14 pixels separation between neighbouring window centroids) and pixel size ranging between 4 to 9 μm.

Table 3 3PB specimen dimensions: width W, thickness B and a_0/W ratio. The span $S = 36.5$ mm and the specimen length $L = 50$ mm

Bone #1				Bone #2			
Spe #	W (mm)	B (mm)	a_0/W	Spe #	W (mm)	B (mm)	a_0/W
3	3.25	3.07	0.31	1	3.71	2.78	0.32
4	4.23	3.31	0.34	2	3.79	2.81	0.28
5	3.34	3.12	0.35	3	4.03	2.71	0.30
6	4.25	3.10	0.23	4	4.36	3.03	0.31
7	4.25	3.00	0.23	5	3.52	2.70	0.34
8	3.99	3.50	0.26	6	4.76	2.88	0.18
10	4.45	3.58	0.20	7	4.43	2.92	0.32
11	3.67	3.10	0.31	8	3.96	3.08	0.26
12	4.70	3.75	0.22	9	4.60	2.69	0.26
13	4.05	3.84	0.26	10	4.33	2.98	0.32
14	4.92	3.86	0.26	11	4.26	2.83	0.32
16	3.96	3.26	0.32	12	4.36	3.12	0.28
18	3.82	3.10	0.21	13	5.22	3.11	0.22
19	4.36	3.68	0.27	14	4.10	2.85	0.32
20	4.77	3.62	0.32	15	4.85	2.82	0.21
21	3.74	2.93	0.22	16	4.74	3.02	0.28
22	3.66	2.83	0.24	17	4.73	3.15	0.30
23	4.05	3.30	0.32	18	4.03	2.96	0.34
24	3.98	2.63	0.26	19	4.16	2.81	0.26
25	3.72	2.64	0.33	20	4.47	2.79	0.28
26	3.71	2.83	0.40	21	4.06	2.54	0.27
27	3.29	2.59	0.32	22	3.34	2.82	0.25
29	3.21	2.55	0.35	23	3.77	3.01	0.34
30	3.15	2.67	0.38	24	4.66	2.92	0.23
				25	4.64	2.81	0.28
				26	4.45	3.03	0.29
				27	3.94	2.92	0.27
				28	4.32	2.91	0.32
				29	4.80	2.96	0.38
				30	3.86	2.87	0.38
				31	3.15	2.75	0.34
				32	3.89	2.91	0.26
				33	4.14	2.78	0.31
				34	3.18	2.90	0.35

predicts the fracture load in the FEA (that mimics a 3PB experiments) should be recommended. We validated that the load-line displacement (LLD) measured by the Instron machine corresponded to the displacement U_t applied in the finite element (FE) model. We used DIC measurements of the vertical displacement at three different points on 3PB specimens and compared them to the vertical displacement measured by the Instron machine as shown in Fig. 12b. Any initial zero displacement of the Instron machine associated with a null force was removed during post-processing of the experiments.

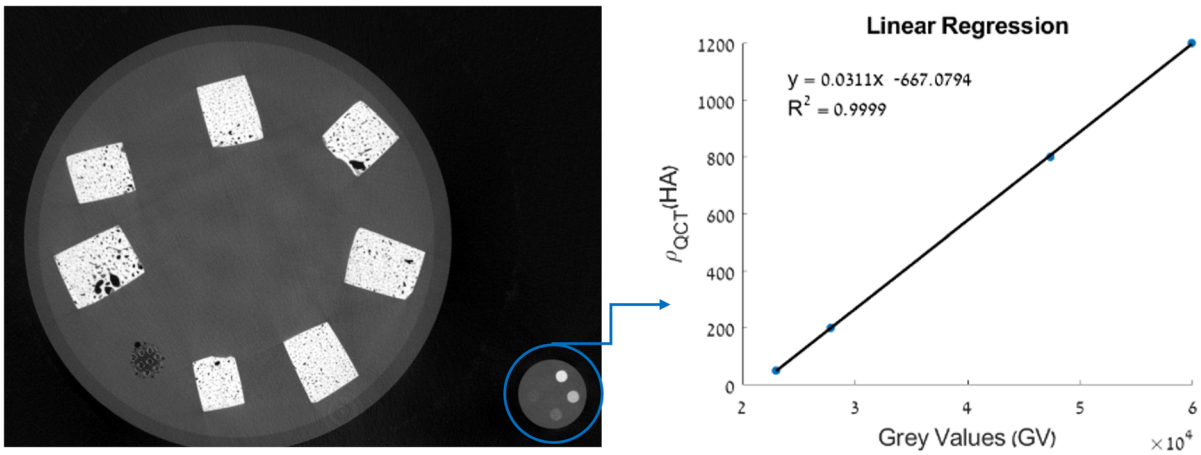

Fig. 8 Micro-CT scan of the notched bone specimens and calibration of μCT GVs with HA phantoms

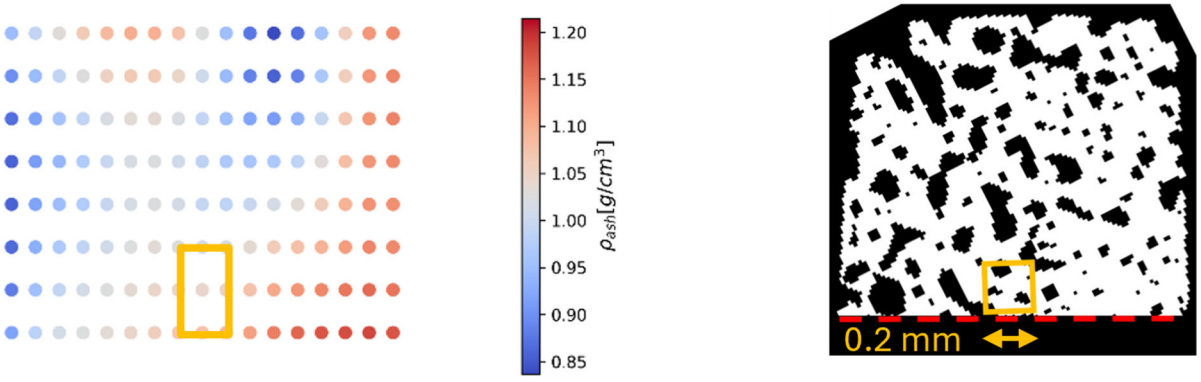

(a) Spe 9 - ρ_{ash} (qCT) (b) Spe 9 - porosity (μCT)

Fig. 9 Comparison between ρ_{ash} distribution and porosity of 2D slices along the notch front extracted from clinical qCT and segmented μCT images, respectively. The yellow square indicates the size of the 2D area i.e $0.2 \times 0.2\ mm^2$ and the notch front is indicated by a dashed red line

3 Experimental results

3.1 Measured K_{Ic}

The *ASTM* and *RILEM* standards assume specimens made of a homogeneous and isotropic material and subjected to plane-strain loading conditions. *ASTM* also involves the calculation of the load P_Q and $P_{max}/P_Q \leq 1.1$ to ensure linear elastic behavior. *RILEM* is based on the maximum force P_{max}. Determining K_{Ic} based on v we observed $P_{max}/P_Q^v > 1.1$ for most of the specimens indicating non-linearities. Determining K_{Ic} based on COD we observed $P_{max}/P_Q^{COD} > 1.6$ for most of the specimens. We first present the correlation between K_{Ic} vs. ρ_{ash} using the power function for all the specimens considered and using v and COD as displacement measurements. The results of the experiments from the different methods and their details are reported in Appendices A and B (Tables 6, 7, 8 and 5).

Considering COD as displacement measurement, RILEM results in higher fracture toughness values. It is coherent to the purpose of this method giving less conservative values than standard methods. However the use of P_{max} instead of P_Q^v with ASTM gives similar results compared to the RILEM applied using v as displacement measurement (see Fig. 13). We also remark

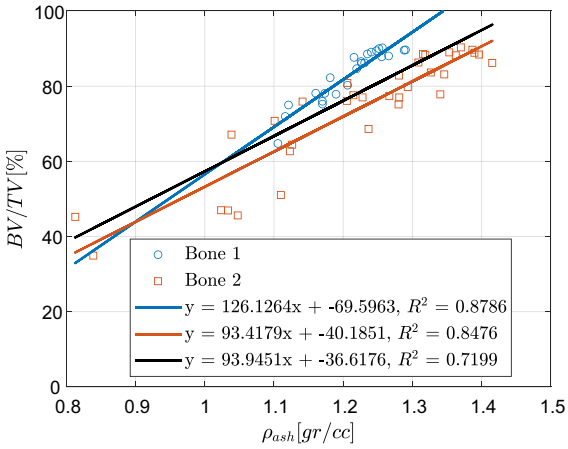

Fig. 10 Correlations between calculated BV/TV and qCT-based ρ_{ash} density for bone #1 (in blue), bone #2 (in orange) and both bones (in black)

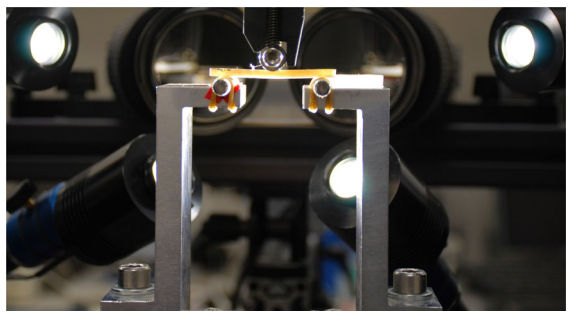

Fig. 11 Typical 3PB experimental setup of a notched bone specimens with DIC

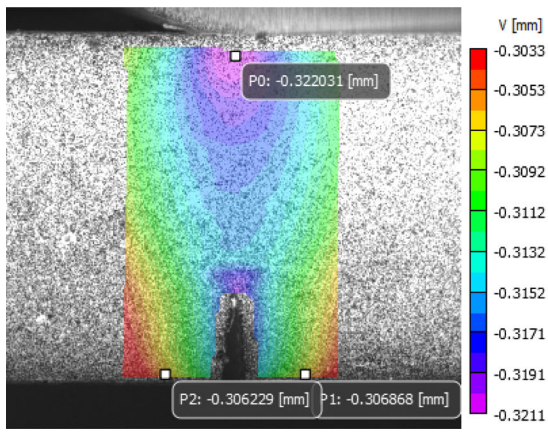

(a) v from DIC

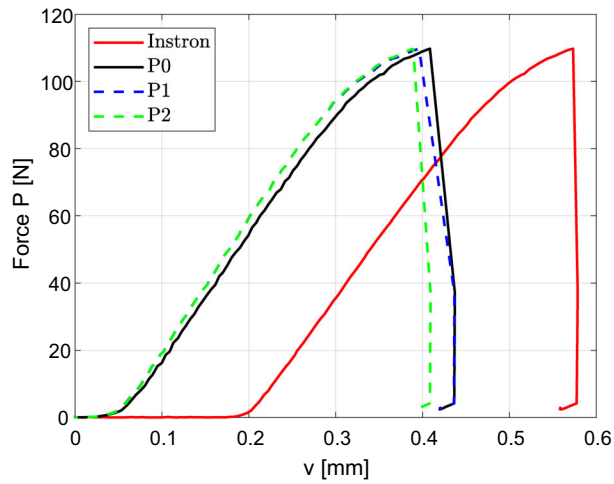

(b) Comparison Instron/DIC

Fig. 12 Comparison between the LLD from the Instron machine and the vertical displacement measured by DIC at three points on the specimen indicated in (**a**)

that RILEM method in not applicable for all the specimens so the R^2 could be slightly higher than the ones resulting from ASTM method. Due to non-linearities in the COD, P_Q^{COD} values and so K_{Ic} values are lower (see Fig. 14) using COD as displacement measurement with ASTM method. It may also explain the difference in the power coefficients of the correlations with the RILEM method.

3.2 K_{Ic} values vs. ρ_{ash} density

Graphs presenting K_{Ic} as a function of ρ_{ash} are given in Figs. 13 and 14.

3.3 G_{Ic} as a function of ρ_{ash}

Assuming plane-strain conditions:

$$G_{Ic} = \frac{K_{Ic}^2(1-\nu^2)}{E} \tag{2}$$

Using the validated $E(\rho_{ash})$ correlation for human cortical bone (Keller 1994):

$$E(\rho_{ash}) = 10200\rho_{ash}^{2.01} \quad [MPa] \quad R^2 = 0.669 \tag{3}$$

In (2) and assuming Poisson's ratio $\nu = 0.3$, one obtains:

$$G_{Ic}(\rho_{ash})[N/m] = \frac{K_{Ic}^2(\rho_{ash})(1-\nu^2)}{10200\rho_{ash}^{2.01}} \cdot 10^6 \quad \text{with } \rho_{ash} \text{ in } gr/cc \tag{4}$$

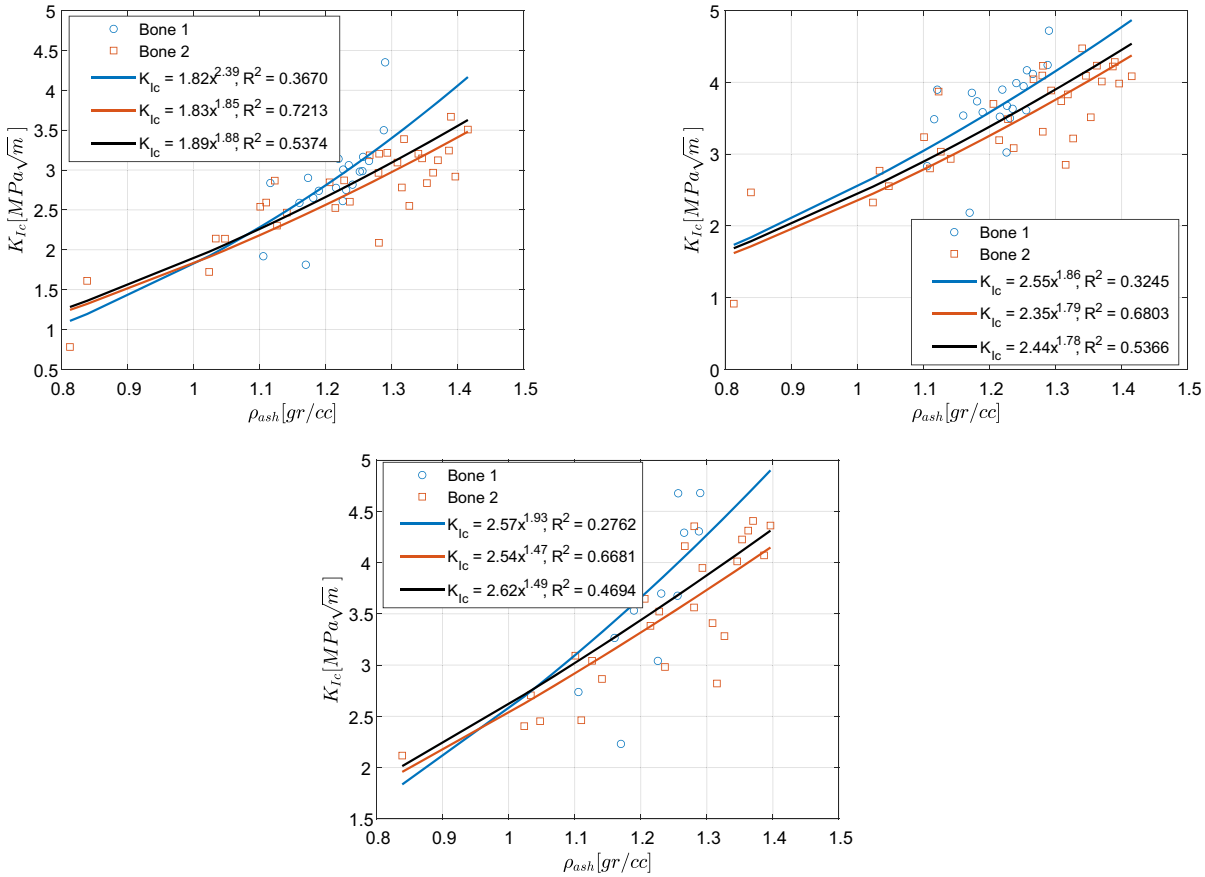

Fig. 13 K_{Ic} vs ρ_{ash} correlation by LLD (v). Upper left *ASTM*, Upper right *ASTM* using P_{max} instead of P_Q^v, Down *RILEM*. Bone #1 (blue, circles), bone #2 (orange, squares) and both bones (black)

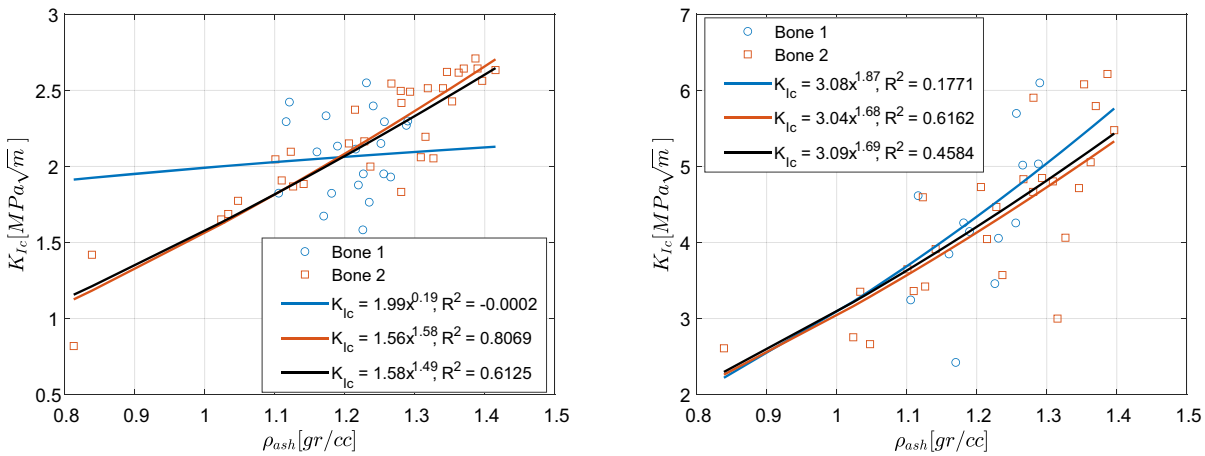

Fig. 14 K_{Ic} vs ρ_{ash} correlation by COD. Left *ASTM*, Right *RILEM*. Bone #1 (blue, circles), bone #2 (orange, squares) and both bones (black)

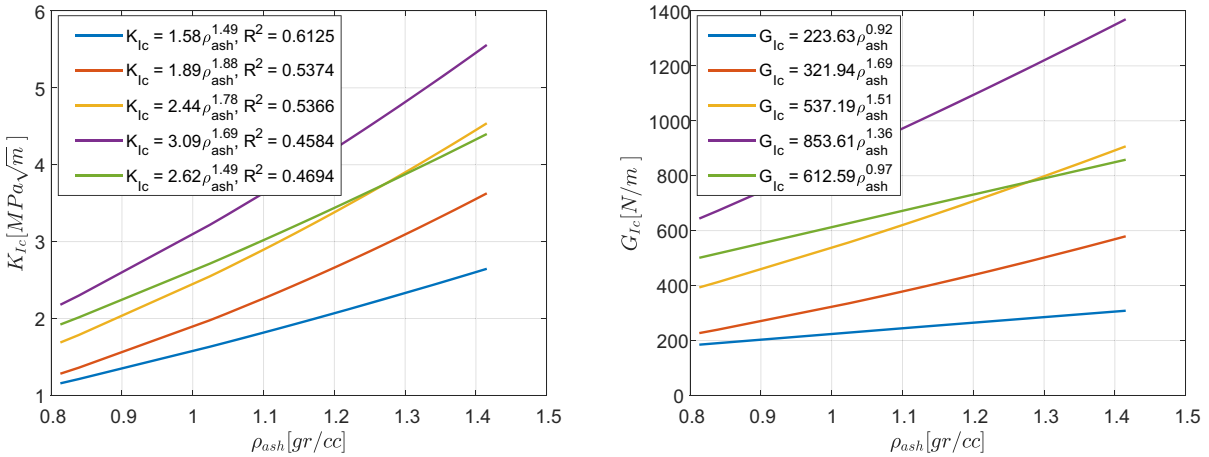

(a) K_{Ic} vs. ρ_{ash} (b) G_{Ic} vs. ρ_{ash}

Fig. 15 Correlations between ρ_{ash} and (**a**) K_{Ic}, (**b**) G_{Ic} estimated from experimental results

Table 4 Summary of the relationships $K_{Ic}(\rho_{ash})$, correlation coefficients R^2 and $G_{Ic}(\rho_{ash})$. The ash density ρ_{ash} is expressed in gr/cc

Method	$K_{Ic}(\rho_{ash})$ $[MPa\sqrt{m}]$	R^2	$G_{Ic}(\rho_{ash})$ $[N/m]$
ASTM, COD	$K_{Ic} = 1.58\rho_{ash}^{1.49}$	0.6125	$G_{Ic} = 223.63\rho_{ash}^{0.92}$
ASTM, v	$K_{Ic} = 1.89\rho_{ash}^{1.88}$	0.5374	$G_{Ic} = 321.94\rho_{ash}^{1.69}$
ASTM (P_{max}), v	$K_{Ic} = 2.44\rho_{ash}^{1.78}$	0.5366	$G_{Ic} = 537.19\rho_{ash}^{1.51}$
RILEM, COD	$K_{Ic} = 3.09\rho_{ash}^{1.69}$	0.4584	$G_{Ic} = 853.61\rho_{ash}^{1.36}$
RILEM, v	$K_{Ic} = 2.62\rho_{ash}^{1.49}$	0.4694	$G_{Ic} = 612.59\rho_{ash}^{0.97}$

The resulting correlations $K_{Ic}(\rho_{ash})$ for the specimens from the two bones and $G_{Ic}(\rho_{ash})$ are presented graphically in Fig. 15 and summarized in Table 4.

Five correlations have been estimated from the different experimental techniques. The most appropriate one for predicting fracture load of human cortical bone tissue was yet to be determined. This was accomplished by FE analyses that mimic the 3PB experiments, employing the phase-field method and the five $G_{Ic}(\rho_{ash})$ correlations reported in Table 4.

4 FEAs to determine the appropriate $G_{Ic}(\rho_{ash})$ correlation

Among the five different $G_{Ic}(\rho_{ash})$ correlations, one should identify the "most appropriate" one - i.e. the correlation that may predict by a FE analysis, implementing the PFM, the 3PB experimental observations. We selected the linear elastic AT1 PFM model for a heterogeneous domain (Levy et al. 2024). Considering the 2D plane-strain domain Ω, $\underline{x} \in \Omega$ and the boundary conditions presented in Fig. 16 we minimized with respect to $\underline{u}$ and $\alpha \in [0, 1]$ the functional:

$$\Pi(\underline{u}, \alpha) = \int_{\Omega} \frac{1}{2} \underline{\underline{\sigma}}(\underline{u}, \alpha) : \underline{\underline{\varepsilon}}(\underline{u}) d\Omega + C \int_{\Omega} \frac{G_{Ic}(\rho_{ash}(\underline{x}))}{l_0} \left(\alpha + l_0^2 ||\underline{\nabla} \alpha||^2 \right) d\Omega \tag{5}$$

Where $\underline{u}$ is the displacement field, $\underline{\underline{\varepsilon}}$ is the strain tensor and $\underline{\underline{\sigma}}$ the stress tensor of the material expressed as

$$\underline{\underline{\sigma}}(\underline{u}, \alpha) = \left[(1 - \alpha)^2 + k_{res} \right] \underline{\underline{\sigma}}^0(\underline{u}) \tag{6}$$

with $\underline{\underline{\sigma}}^0$ corresponding to the stress field associated with the undamaged state defined in (7) and $\alpha \in [0, 1]$ is the

damage field, the value 0 corresponds to the undamaged state whereas the value 1 corresponds to the fully damaged state. $k_{res} \ll 1$ is a small parameter avoiding a zero stiffness.

$$\underline{\underline{\sigma}}^0(\underline{u}) = \lambda tr(\underline{\underline{\varepsilon}}(\underline{u}))\underline{\underline{I}} + 2\mu\underline{\underline{\varepsilon}}(\underline{u}) \quad in \quad \Omega \tag{7}$$

λ and μ the Lamé parameters that are obtained from the Young's modulus (3) and the Poisson's ratio (ν) by the following relations:

$$\lambda = \frac{E(\rho_{ash}(\underline{x}))\nu}{(1+\nu)(1-2\nu)}, \quad \mu = \frac{E(\rho_{ash}(\underline{x}))}{2(1+\nu)} \tag{8}$$

Remark 4.1 We use the AT1 value $C = 3/8$ in (5) although this value was determined under the assumptions of a homogeneous 1D bar and has not yet been thoroughly investigated for a heterogeneous G_{Ic} changing along the crack path in 2D domain.

For the AT1 model (5) was minimized imposing the irreversibility constraint (9) also referred as *no-healing* condition:

$$\dot{\alpha} \geq 0 \tag{9}$$

5 PFM–FEA

To mimic the 3PB experiments, plane-strain FE analyses were performed using FEniCSx (Langtangen and Logg 2017) (see Fig. 16), with specimen lengths of $L^{sym} = L/2 = 25$ mm and symmetric boundary conditions. An unstructured mesh was used having linear triangular elements (TRI3) and mesh refinement $h \in [h_{min}, h_{max}]$ was applied such that $h_{max} = 0.125 = L^{sym}/200$. The area of the notch tip was highly refined. Displacement boundary conditions $u_y = U_t$ and $u_y = 0$ in Fig. 16 were applied over lengths of 0.5 and 1 mm, respectively. To ensure numerical convergence, we use a refinement ratio of $\ell_0/h_{min} = 10$ in the actual/potential crack region and element size h_{top} varying from $y_0/80$ to $y_0/800$ in the area where vertical displacement is applied. $y_0 = W/8$ is the length of the surface on which the force is applied. A staggered solution scheme with an error tolerance of 10^{-5} was used for coupling of elastic and PF solutions. The SNES and TAO solvers were used enforcing the irreversibility condition (9) by the Active Set Method.

Four 3PB specimens were chosen arbitrarily, covering a span of densities (#18 from bone #1 and #13, #28, #29 from bone #2), to investigate if among the five different $G_{Ic}(\rho_{ash})$ correlations there exists one which best fits the experimental observations. The ρ_{ash} distribution in the $y-$direction was determined based on the qCT scan using a power fitting method. The four specimens had the notch in the inner part (trabecular) so the crack is propagating towards the outer stiffer part (cortical) as ρ_{ash} increases, as presented in Fig. 17a. No ρ_{ash} variation in the longitudinal x-direction was considered, as it is almost constant in the notch region. Consequently, E and G_{Ic} are spatially distributed only along the crack propagation direction (y). The force P^{FE} was computed where the displacement U_t was applied. The loading history was defined as $U_t = \{0, \Delta_t, 2\Delta_t, ..., n\Delta_t\}$ with $\Delta_t = -0.005$ mm. n was determined so the FE analysis stopped at a 5% decrease of the calculated force P^{FE}.

For the AT1 model, ($\alpha = 1$) is prescribed on the notch faces as boundary conditions (Tanné et al. 2018).

The FE maximum force $P^{FE}_{\max}$ is reported, because a brittle fracture was noticed in the FEA, thus P^{FE}_{Q} is irrelevant. Investigation of the ℓ_0 influence on $P^{FE}_{\max}$ shows a negligible effect (as expected for crack propagation because ℓ_0 affects crack nucleation (Tanné et al. 2018)). $P^{FE}_{\max}$ vs ℓ_0 for the four specimens is shown in Fig. 17b. Across the four specimens, only a $1-2.5\%$ increase in P_{max} is observed when ℓ_0 is halved. We chose the smallest value $\ell_0 = 0.0125$ mm in our PF analyses.

Remark 5.1 Numerical corrections of G_{Ic} to account for l_0/h, such as reported in Levy et al. (2024), were investigated, showing to have minor effect on the FE results because of the high l_0/h_{min} values.

The force-displacement curves obtained using the five $G_{Ic}(\rho_{ash})$ correlations for each specimen were compared to the experimental $P(v)$ data in Fig. 18.

In Fig. 19 we illustrate the relative difference in the predicted fracture forces P^v_Q and P^{EXP}_{max} for each specimen using the various $G_{Ic}(\rho_{ash})$ correlations.

It is observed that the correlation $G_{Ic} = 321.94\rho^{1.69}_{ash}$ predicts the experimental maximum force P^{EXP}_{max} within a 5% error range for three out of the four specimens (see Fig. 19b). For specimen #13 the relative error in predicting P^{EXP}_{max} exceeds 10% but this correlation accurately predicts the P^v_Q force within a 5% error range (see Fig 19a). Therefore, $G_{Ic} = 321.94\rho^{1.69}_{ash}$ is identified as the most appropriate correlation.

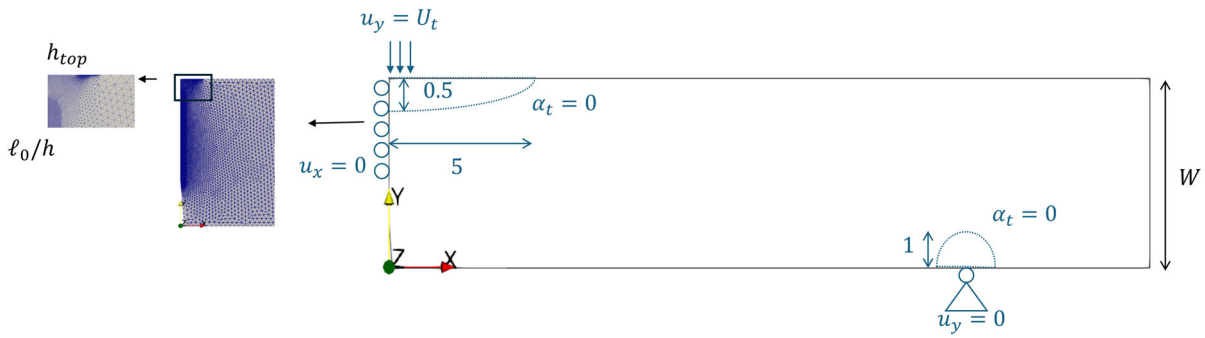

Fig. 16 Right: FE model and boundary conditions of the 3PB experiment. The FE models are 25 mm in length and the half-span is 18.25 mm. Left: The FE refined mesh along the anticipated crack path

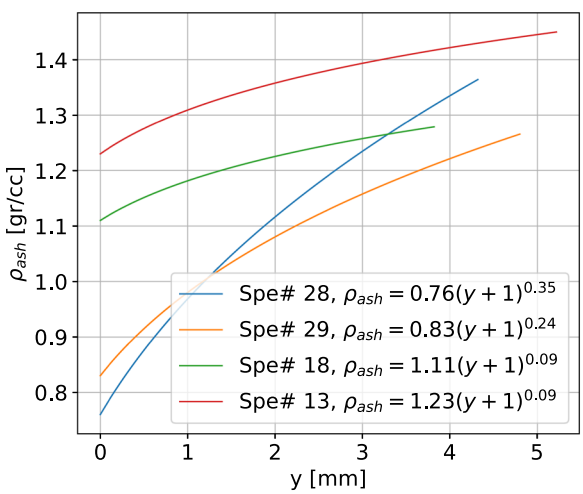

(a) $\rho_{ash}(y)$

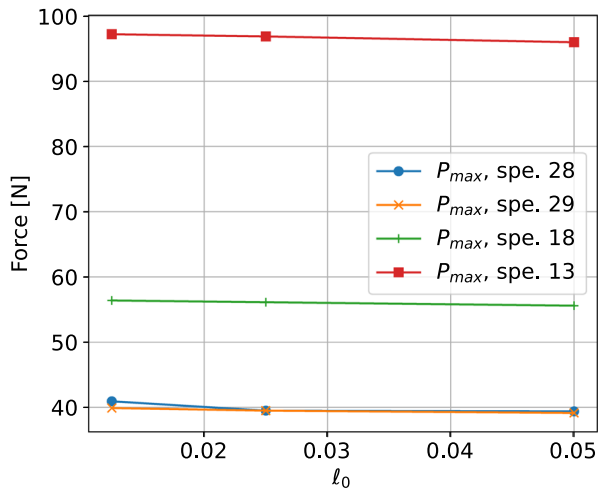

(b) $\ell_0/h_{min} = 10$, fixed

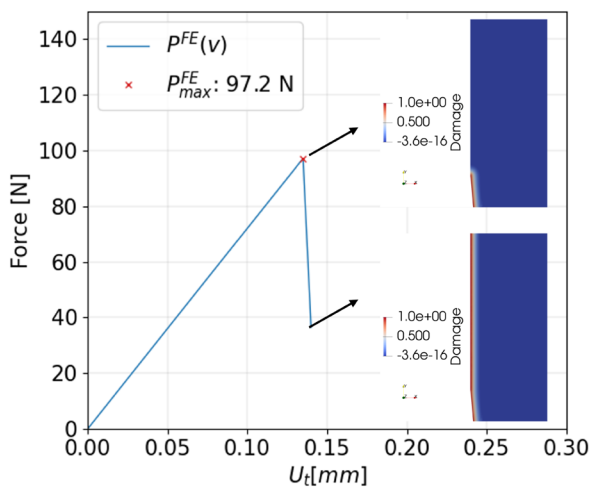

(c) U_t vs P

Fig. 17 **a** $\rho_{ash}(y)$ in the y-direction of the four 3PB specimens. **b** Sensitivity analysis for ℓ_0, $\ell_0 = 0.05, 0.025, 0.0125$ mm. **c** Force versus displacement for $\ell_0 = 0.0125$ mm, and specimen #13. The correlation $G_{Ic}(\rho_{ash}) = 321.94\rho_{ash}^{1.69}$ is used in (**b**) and (**c**)

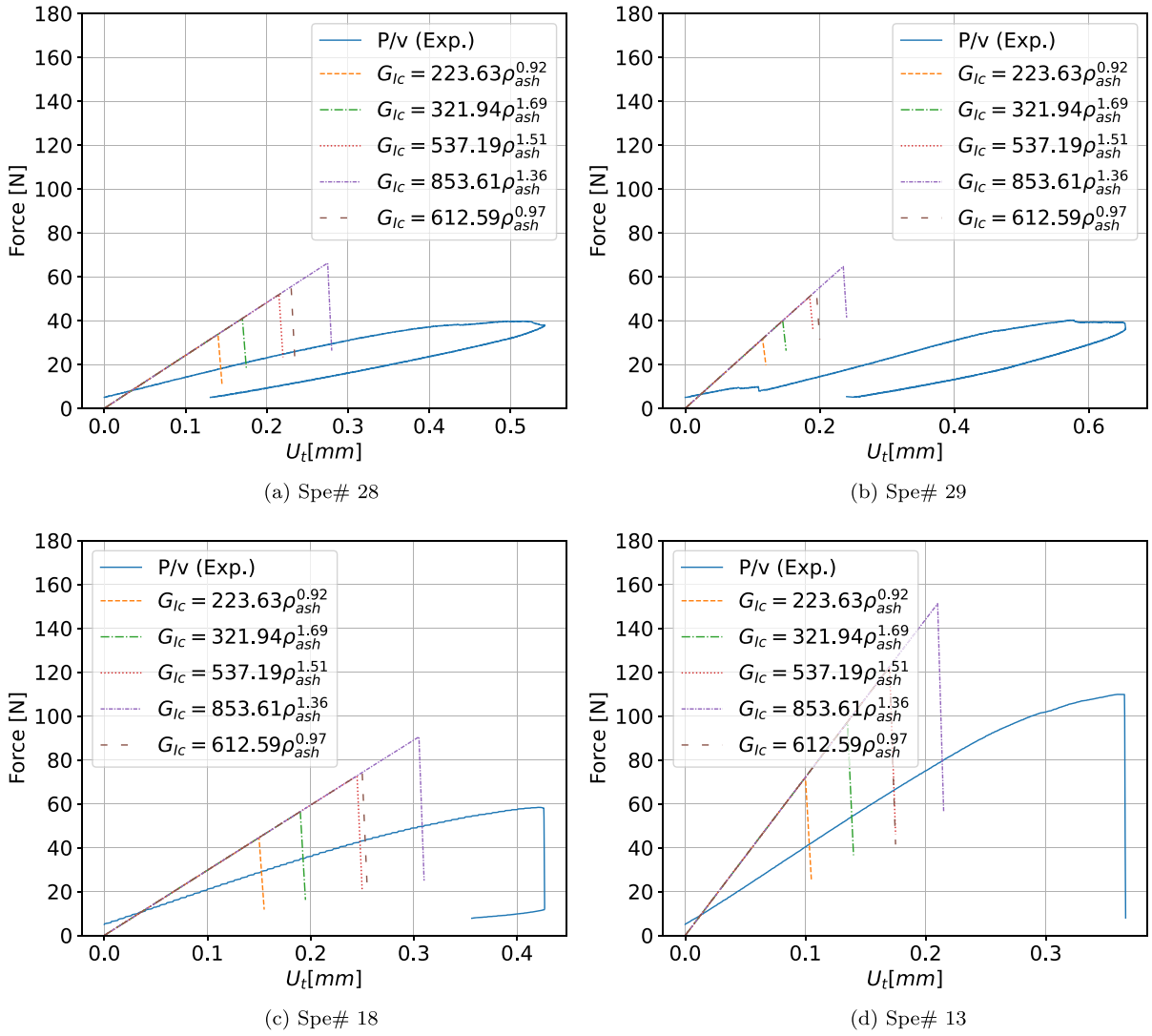

(a) Spe# 28

(b) Spe# 29

(c) Spe# 18

(d) Spe# 13

Fig. 18 Comparison between experimental (Instron) force-displacement curves and FEA computed ones for the four specimens

Although the computed maximum force well predicts the experimental observations, the force-displacement slopes in Fig. 18 overestimate the experimental ones.

In the experimental setting, a rigid body deflection of the specimen may occur due to the soft bone tissue residing on the two steel cylinders used as a support. To eliminate this unknown rigid body-motion (not simulated by the FEA), we considered the force-strain response. The ε_{xx} strain measured by DIC at a point P0 (see Fig. 20a) on specimen #13 was compared to the FEA computed strain in Fig. 20b. One may observe a much better match of the slopes, indicating as expected a rigid body motions and additional vertical displacement due to the 3PB test setup. This analysis was performed for the three other specimens obtaining similar results, suggesting a possible mismatch between the boundary conditions applied in the FEA and the experimental ones.

The complex microstructure of bone results in crack tortuosity. Examining the evolution of the measured DIC ε_{xx} for sample #13, for example, as shown in Fig. 21, the onset of damage is observed (particularly in Fig. 21b) at a force between P_Q^v and P_{max}^{EXP}. The specimen fractures immediately after $P = P_{max}^{EXP}$, exhibiting tortuosity (see Fig. 21d), which may be related to the

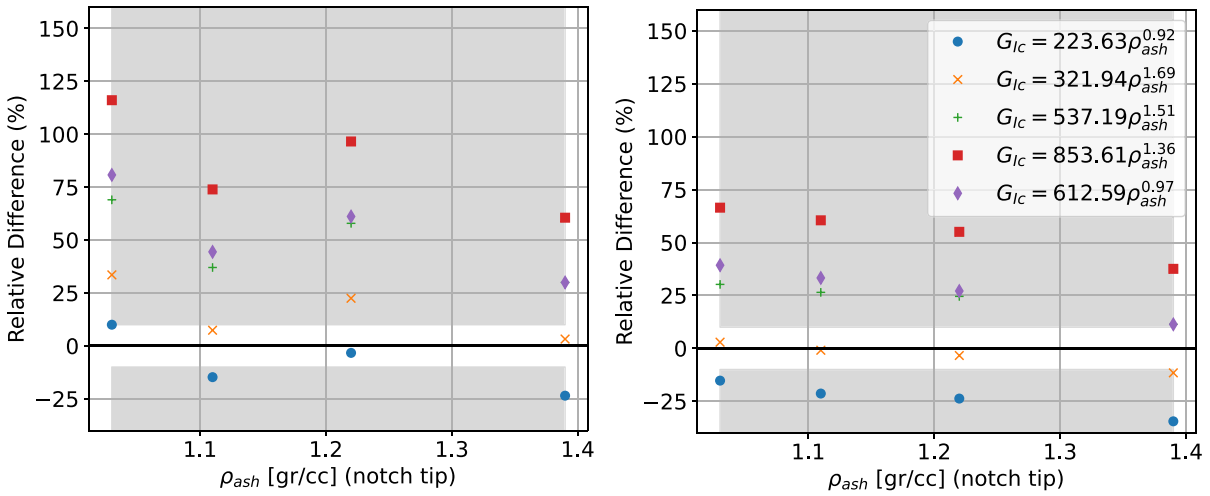

(a) P_{max}^{FE} vs. P_Q^v (b) P_{max}^{FE} vs. P_{max}^{EXP}

Fig. 19 Relative difference between P_{max}^{FE} and P_Q^v, P_{max}^{EXP} measured from the experiments using v as displacement measurement for the 4 specimens (Spe# 28, 29, 18, 13, left to right) and the 5 correlations: $G_{Ic} = 223.63\rho_{ash}^{0.92}$ (∘), $G_{Ic} = 321.94\rho_{ash}^{1.69}$ (×), $G_{Ic} = 537.19\rho_{ash}^{1.51}$ (+), $G_{Ic} = 853.61\rho_{ash}^{1.36}$ (□), $G_{Ic} = 612.59\rho_{ash}^{0.97}$ (◊)

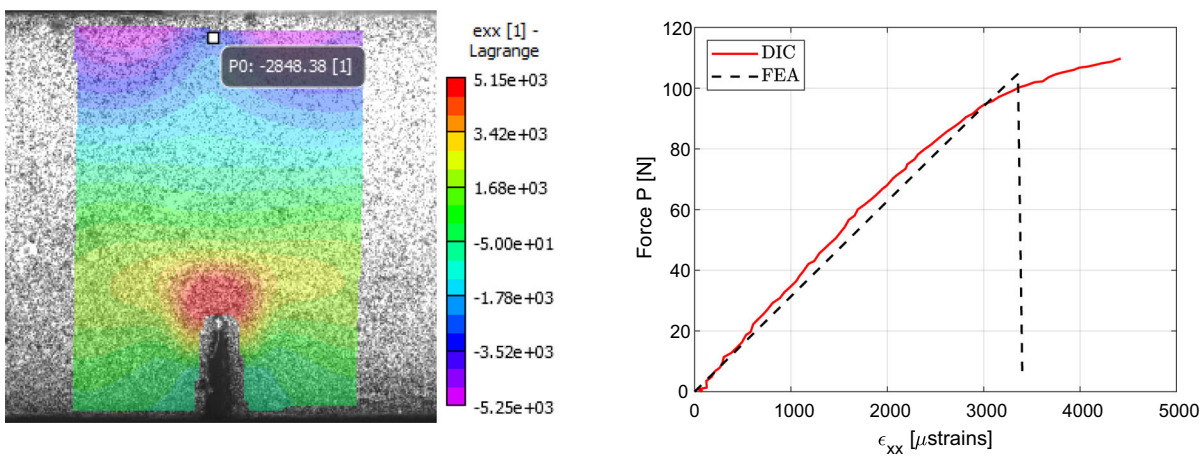

(a) ε_{xx} [μstrains] from DIC (b) Comparison DIC/FEA

Fig. 20 ε_{xx} measured by DIC at the point P0 on specimen #13. A filter size of 25 was used with Vic3D (**a**). Force vs. ε_{xx} - Experiment and calculated by FEA using $G_{Ic} = 321.94\rho_{ash}^{1.69}$ (**b**)

toughening mechanisms described in the literature for cortical bone fracture (Nalla et al. 2005; Ritchie et al. 2009; Zimmermann et al. 2010; Libonati and Vergani 2016). This behavior was observed in the DIC images for most specimens.

Hence, the use of ASTM standards with P_{max}^{EXP} instead of P_Q^v may overestimate K_{Ic} values, which explains the overestimation of P_{max}^{EXP} in FEA using the associated correlation $G_{Ic}(\rho_{ash})$. Using RILEM standards with v as the displacement measurement leads to similar results.

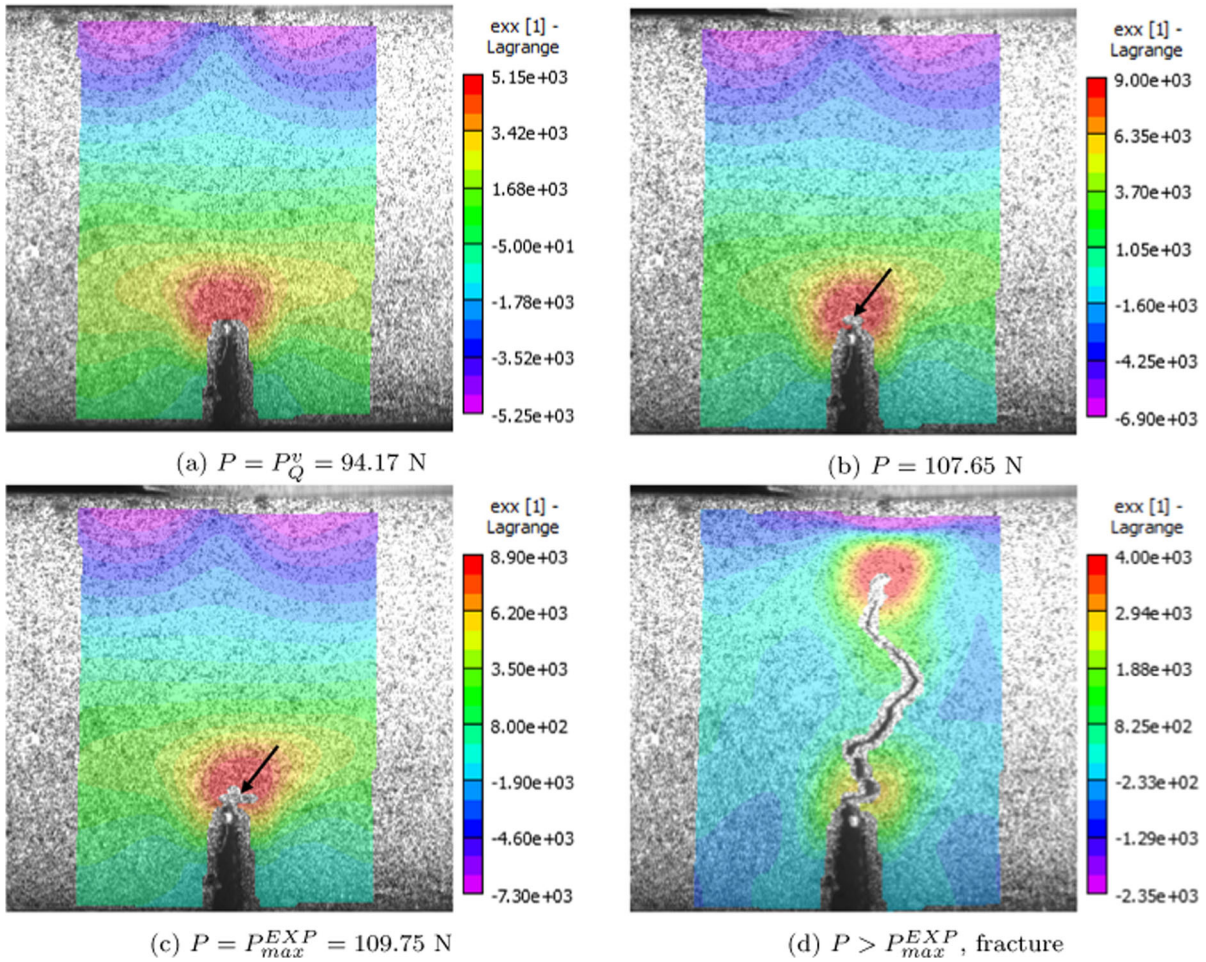

Fig. 21 Evolution of the strains ε_{xx} [μstrains] measured by DIC from $P = P_Q^v$ to fracture ($P > P_{max}^{EXP}$) for specimen #13. A filter size of 25 was used to calculate the strains with Vic3D (DIC). The damage initiation (loss of data points) is indicated with a black arrow

6 Uncertainty quantification for $G_{Ic}(\rho_{ash})$ correlation

The scattering of experimental data for the averaged correlation $G_{Ic} = 321.94\rho_{ash}^{1.69}$ was expected for the biological tissue, see Figs. 13 and 14. A random-field analysis for $K_{Ic}(\rho_{ash})$ and $G_{Ic}(\rho_{ash})$ relationships was performed (see Appendix C), and the implied influence on the variance in the maximum force P_{max}^{FE} was computed.

Following (Wille et al. 2012) a *stochastic* relationship $K_{Ic} - \rho_{ash}$ was formulated, determining the two standard deviations upper and lower values ($K_{Ic}^{upper}(\rho_{ash})$ and $K_{Ic}^{lower}(\rho_{ash})$), so 95.4% of the experimental data are between the bounds) for the $K_{Ic} = 1.89\rho_{ash}^{1.88}$ correlation (see Fig. 22a). Based on it, the *stochastic* relationship

$$G_{Ic} = 321.94\rho_{ash}^{1.69} \cdot exp(\pm 2SD) \tag{10}$$

was also determined obtaining $SD = 0.30$. The lower and upper bounds for $G_{Ic} - \rho_{ash}$ relationship are depicted in Fig. 22b. These correlations are implemented in the PFM analysis to evaluate the interval of confidence associated with P_{max}^{FE}, the fracture force predicted by the PFM.

One may note the excellent correlation of the computed mean value for fracture when compared to the experimental maximum load at fracture, and the increase in the uncertainty for the higher ash density values (see Fig. 23).

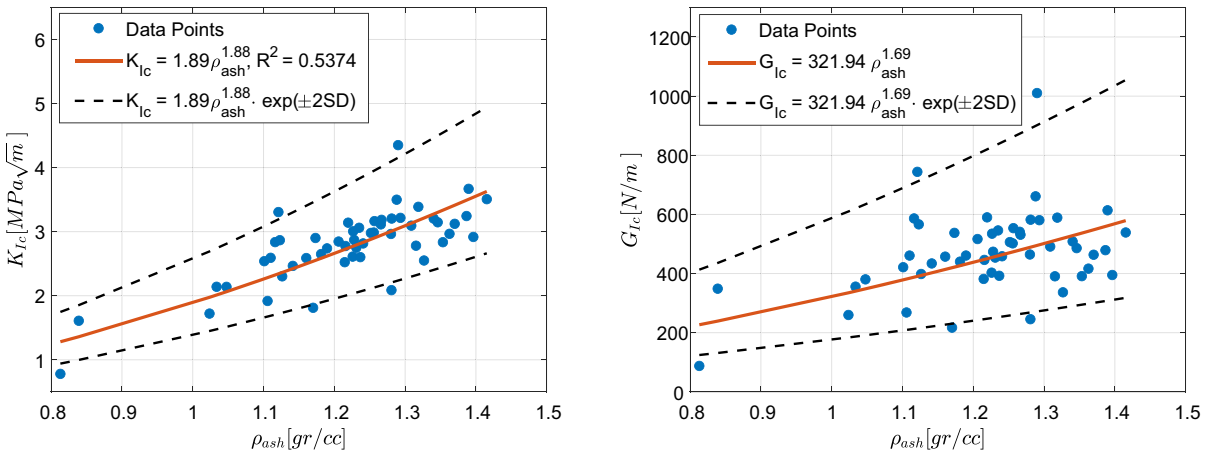

(a) K_{Ic} vs. ρ_{ash} (b) G_{Ic} vs. ρ_{ash}

Fig. 22 Upper and lower 2SD bounds for **a** K_{Ic}, **b** G_{Ic}. SD for K_{Ic} is 0.15 and SD for G_{Ic} is 0.30

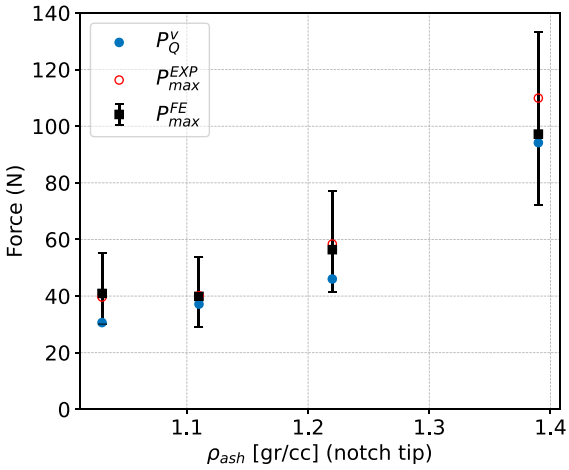

Fig. 23 PFM average, upper and lower bounds ($\pm 2SD$) for the computed fracture load (P_{max}^{FE}) for the four randomly selected specimens, compared to the experimental values

7 Summary and conclusions

Five experimental techniques were investigated to obtain a K_{Ic} vs. ρ_{ash} correlations, resulting in five $K_{Ic}(\rho_{ash})$ relationships with $R^2 = 0.46 - 0.61$. QCT scans of the entire bone followed by μCT of the extracted specimens allowed for the determination of ρ_{ash} in the notch front, ensuring minimal variation along the notch. The correlations from bone #2 were more significant due to a broader density range and better specimen preparation, leveraging the experience from bone #1.

In the L-R orientation, the ASTM standard using displacement at the force application point and P_Q was found to be the recommended experimental method, obtaining K_{Ic} in the range 0.78 - 4.35 MPa$\sqrt{m}$ similar to the literature range of 2.2-7 MPa$\sqrt{m}$. It is important to note that many values in past literature used maximum force and different orientations. The fracture toughness range for $\rho_{ash} = 0.81 - 1.42$ gr/cc was $G_{Ic} = 88 - 1010$ N/m, comparable to data in past literature for human long bones (in the L-C orientation), reported to be $150 - 830$ N/m (Norman et al. 1995; Yeni et al. 1998; Yeni and Norman 2000b).

To the best of our knowledge, the only existing correlation $G_{Ic}(\rho_{ash})$ (in L-C orientation) was provided by Yeni et al. (1998), with $R^2 = 0.20 - 0.35$. Therefore, our results appear to be the most significant reported to date.

Validating the $G_{Ic}(\rho_{ash})$ correlations with FE analyses for four randomly selected specimens identified the correlation $G_{Ic} = 321.94\rho_{ash}^{1.69}$ as the most appropriate to reproduce experimental results in terms of P_{max}. This correlation followed the ASTM standard, considering v as the displacement measurement. A statistical analysis was also performed, assuming a normal distribution, resulting in lower and upper bounds for $G_{Ic}(\rho_{ash})$ with a standard deviation of 0.30, i.e. for a 95.4% confidence interval $G_{Ic} = 321.94\rho_{ash}^{1.69} \cdot exp(\pm 2SD)$.

Limitations:

Several limitations are important to notice.

- Although a large number of samples were tested, they were extracted from two donors, while previous studies have reported results based on 10

(Zioupos and Currey 1998) to more than 30 donors (Yeni et al. 1998; Wang et al. 2002; Granke et al. 2015).
- There were few specimens with low ρ_{ash} values.
- Bone fracture toughness may be dependent on other parameters as environment (Shin et al. 2022), aging (Zioupos and Currey 1998; Koester et al. 2011), microstructural parameters like porosity and osteon density (Yeni et al. 1997), cement lines (Yeni and Norman 2000a), and compositional parameters such as water content (Granke et al. 2015), collagen integrity (Wang et al. 2002), and tissue heterogeneity (Katsamenis et al. 2015). These parameters were not considered in our investigation.
- The finite element analysis (FEA) was conducted without incorporating multi-scale modeling approaches. As a result, toughening mechanisms such as crack deflection and other microstructure-related effects in cortical bone, which may influence the experimental results, were not explicitly accounted for in the simulations.

Acknowledgements The authors acknowledge the support of the European Union's Horizon 2020 research and innovation programme under the Marie Sklodowska-Curie grant agreement No. 861061 - NEWFRAC, and the support of the Israel Science Foundation (grant No. 1748/24).

Author contributions ZY and ML wrote the main manuscript text. ZY and ML reviewed the manuscript.

Funding Open access funding provided by Tel Aviv University.

Data Availability Statement No datasets were generated or analysed during the current study.

Declarations

Conflict of interest The authors declare no Conflict of interest.

Appendix A Experimental results using *ASTM* standards

Table 5 a_c and K_{Ic} values calculated from specimens of bone 2# with *RILEM* standards (RILEM-TC-089-FMT 1991) using LLD (v) and COD associated with qCT-based density ρ_{ash} and Young modulus E

Spe #	ρ_{ash} $[gr/cc]$	E [GPa]	a_c^{COD}/a_0	a_c^{v}/a_0	$K_{I_c}^{COD}$ $[MPa\sqrt{m}]$	$K_{I_c}^{v}$ $[MPa\sqrt{m}]$
1	1.36	19.22	1.21	1.02	5.06	4.31
2	0.81	6.32	N/A	N/A	N/A	N/A
3	1.14	12.74	1.37	0.97	3.91	2.86
4	1.28	16.14	1.40	1.09	4.67	3.56
5	1.39	19.99	1.41	0.96	6.22	4.07
6	1.23	15.82	1.52	1.02	4.47	3.52
7	1.12	13.20	1.21	0.97	4.59	3.79
8	1.21	14.26	1.38	0.98	4.73	3.65
9	1.35	18.70	1.79	1.28	6.08	4.23
10	1.27	17.37	1.21	1.03	4.83	4.16
11	1.21	15.18	1.28	1.07	4.05	3.38
12	1.33	17.58	1.33	1.03	4.06	3.28
13	1.39	19.95	N/A	N/A	N/A	N/A
14	1.10	13.92	1.15	0.94	3.65	3.09
16	1.35	18.54	1.21	0.97	4.72	4.01
17	1.37	19.13	1.47	1.12	5.79	4.41

Table 5 continued

Spe #	ρ_{ash} $[gr/cc]$	E [GPa]	a_c^{COD}/a_0	a_c^{v}/a_0	$K_{I_c}^{COD}$ $[MPa\sqrt{m}]$	$K_{I_c}^{v}$ $[MPa\sqrt{m}]$
18	1.28	17.22	N/A	N/A	N/A	N/A
19	1.29	16.21	1.33	1.02	4.85	3.95
20	1.40	19.60	1.44	1.13	5.48	4.36
21	1.42	20.77	N/A	N/A	N/A	N/A
23	1.13	12.11	1.14	1.00	3.42	3.04
24	1.28	16.05	1.55	1.05	5.90	4.35
25	1.34	18.37	N/A	N/A	N/A	N/A
26	1.24	15.71	1.20	0.98	4.71	3.95
27	1.32	18.01	1.08	0.95	2.75	2.40
28	1.03	11.71	1.18	0.87	3.35	2.46
29	1.11	13.27	1.31	0.85	3.36	2.70
30	0.84	6.76	1.06	0.95	2.61	2.12
31	1.05	10.94	1.18	0.88	4.80	3.41
32	1.32	17.73	N/A	N/A	N/A	N/A
33	1.31	17.73	1.18	1.04	2.75	2.40
34	1.02	10.38	1.18	1.04	4.80	3.41

Table 6 P_Q, P_{max} and K_{Ic} values calculated from specimens of bone 1# with *ASTM* standards (ASTM-E399 1990) using LLD (v) and COD associated with qCT-based density ρ_{ash} and Young modulus E

Spe #	ρ_{ash} $[gr/cc]$	E [GPa]	P_Q^{COD} [N]	P_Q^{v} [N]	P_{max} [N]	$K_{I_c}^{COD}$ $[MPa\sqrt{m}]$	$K_{I_c}^{v}$ $[MPa\sqrt{m}]$	$K_{I_c}^{P_{max}}$ $[MPa\sqrt{m}]$
3	1.29	16.85	22.53	34.73	42.03	2.27	3.50	4.24
4	1.26	16.47	33.50	46.22	60.88	2.29	3.16	4.17
5	1.18	14.51	17.51	25.45	35.98	1.82	2.65	3.74
6	1.26	16.16	35.82	54.82	66.18	1.95	2.99	3.61
7	1.24	15.62	31.22	54.15	64.19	1.76	3.06	3.63
8	1.22	15.21	33.04	55.25	68.51	1.88	3.14	3.90
10	1.29	17.05	56.60	107.14	115.94	2.30	4.35	4.72
11	1.23	15.37	23.75	36.59	44.69	1.95	3.01	3.67
13	1.23	15.39	31.17	51.41	59.44	1.58	2.61	3.02
14	1.27	16.30	50.92	82.13	108.39	1.93	3.11	4.12
16	1.12	12.49	31.67	39.17	48.05	2.29	2.84	3.49
18	1.22	15.72	35.06	46.04	58.20	2.11	2.78	3.52
19	1.25	15.96	44.08	61.07	80.67	2.15	2.98	3.95
20	1.24	15.74	49.42	58.05	81.98	2.40	2.82	3.99
21	1.19	14.81	31.24	40.11	52.48	2.13	2.74	3.58
22	1.12	13.37	31.88	43.50	51.10	2.42	3.31	3.90
24	1.17	14.25	30.94	38.48	51.18	2.33	2.90	3.85
25	1.17	13.76	16.91	18.30	22.08	1.67	1.81	2.18

Table 6 continued

Spe #	ρ_{ash} $[gr/cc]$	E [GPa]	P_Q^{COD} [N]	P_Q^{v} [N]	P_{max} [N]	$K_{I_c}^{COD}$ $[MPa\sqrt{m}]$	$K_{I_c}^{v}$ $[MPa\sqrt{m}]$	$K_{I_c}^{P_{max}}$ $[MPa\sqrt{m}]$
26	1.11	12.48	16.27	17.11	25.37	1.82	1.92	2.83
27	1.16	13.33	17.36	21.43	29.07	2.09	2.59	3.54
30	1.23	15.16	17.47	18.84	23.80	2.55	2.75	3.50

Appendix B Experimental results using *RILEM* standards

Table 7 P_Q, P_{max} and K_{Ic} values calculated from specimens of bone 2# with *ASTM* standards (ASTM-E399 1990) using LLD (v) and COD associated with qCT-based density ρ_{ash} and Young modulus E

Spe #	ρ_{ash} [gr/cc]	E [GPa]	P_Q^{COD} [N]	P_Q^{v} [N]	P_{max} [N]	$K_{I_c}^{COD}$ [MPa$\sqrt{\text{m}}$]	$K_{I_c}^{v}$ [MPa$\sqrt{\text{m}}$]	$K_{I_c}^{P_{max}}$ [MPa$\sqrt{\text{m}}$]
1	1.36	19.22	28.28	32.07	45.74	2.62	2.97	4.23
2	0.81	6.32	10.22	9.74	11.51	0.82	0.78	0.92
3	1.14	12.74	23.74	31.06	36.87	1.88	2.47	2.93
4	1.28	16.14	27.73	31.59	50.01	1.83	2.09	3.31
5	1.39	19.99	24.86	29.76	38.57	2.71	3.24	3.63
6	1.23	15.82	49.95	66.22	80.29	2.17	2.87	3.49
7	1.12	13.20	31.16	42.61	57.40	2.10	2.87	3.87
8	1.21	14.26	33.20	43.92	56.92	2.15	2.85	3.70
9	1.35	18.70	40.94	47.82	59.22	2.43	2.84	3.51
10	1.27	17.37	37.21	46.57	59.03	2.54	3.18	4.04
11	1.21	15.18	31.66	33.67	42.47	2.37	2.52	3.19
12	1.33	17.58	35.25	43.78	55.05	2.05	2.55	3.22
13	1.39	19.95	67.86	94.17	109.75	2.64	3.67	4.28
14	1.10	13.92	26.40	32.75	41.55	2.05	2.54	3.24
16	1.35	18.54	49.57	59.49	77.12	2.62	3.15	3.87
17	1.37	19.13	49.30	58.24	74.66	2.64	3.12	4.01
18	1.28	17.22	30.97	36.77	50.70	2.50	2.96	4.09
19	1.29	16.21	37.48	48.38	58.37	2.49	3.22	3.89
20	1.40	19.60	40.90	46.56	63.45	2.56	2.92	4.09
21	1.42	20.77	33.57	44.71	51.90	2.63	3.03	4.08
23	1.13	12.11	21.40	26.38	34.61	1.87	2.30	3.03
24	1.28	16.05	47.75	63.31	83.37	2.42	3.20	4.23
25	1.34	18.37	42.73	54.46	75.81	2.51	3.20	4.47
26	1.24	15.71	33.48	43.59	51.65	2.00	2.60	3.08
27	1.32	18.01	30.98	39.26	40.02	1.69	1.81	2.33
28	1.03	11.71	24.16	30.64	39.61	1.91	2.14	2.77
29	1.11	13.27	27.35	37.15	39.98	1.42	1.61	2.34
30	0.84	6.76	14.44	16.37	24.97	1.77	2.14	2.55

Table 7 continued

Spe #	ρ_{ash} [gr/cc]	E [GPa]	P_Q^{COD} [N]	P_Q^{v} [N]	P_{max} [N]	$K_{I_c}^{COD}$ [MPa$\sqrt{\text{m}}$]	$K_{I_c}^{v}$ [MPa$\sqrt{\text{m}}$]	$K_{I_c}^{P_{max}}$ [MPa$\sqrt{\text{m}}$]
31	1.05	10.94	14.18	17.09	20.43	1.60	1.82	2.47
32	1.32	17.73	35.46	47.78	53.74	2.14	2.99	3.83
33	1.31	17.73	26.82	40.28	48.61	2.14	2.99	3.83
34	1.02	10.38	13.60	14.18	19.15	1.65	1.72	2.33

Appendix C Stochastic $G_{Ic} - \rho_{ash}$ correlation

After transforming the K_{Ic} experimental data to a double logarithmic scale, we apply the linear regression model:

$$\ln(K_{Ic}) = A^* + B^* \ln(\rho_{ash}) + X, \tag{C.1}$$

where X represents random deviations assumed to be normally distributed, and A^* and B^* are the intercept and slope, respectively. Assuming the residuals r_i follow $Y \sim \mathcal{N}(0, s_Y^2)$, we express the K_{Ic} correlation in the stochastic form:

$$K_{Ic}^{sto} = A\rho_{ash}^{B} \cdot Z, \tag{C.2}$$

Table 8 a_c and K_{Ic} values calculated from specimens of bone 1# with *RILEM* standards (RILEM-TC-089-FMT 1991) using LLD (v) and COD associated with qCT-based density ρ_{ash} and Young modulus E

Spe #	ρ_{ash} [gr/cc]	E [GPa]	a_c^{COD}/a_0	a_c^{v}/a_0	$K_{I_c}^{COD}$ [$MPa\sqrt{m}$]	$K_{I_c}^{v}$ [$MPa\sqrt{m}$]
3	1.29	16.85	1.21	1.02	5.03	4.30
4	1.26	16.47	1.33	1.12	5.70	4.68
5	1.18	14.51	1.14	1.00	4.26	3.74
6	1.26	16.16	1.28	1.03	4.26	3.68
7	1.24	15.62	N/A	N/A	N/A	N/A
8	1.22	15.21	N/A	N/A	N/A	N/A
10	1.29	17.05	1.50	0.98	6.10	4.68
11	1.23	15.37	N/A	N/A	N/A	N/A
13	1.23	15.39	1.20	1.01	3.46	3.04
14	1.27	16.30	1.30	1.06	5.02	4.29
16	1.12	12.49	1.56	1.09	5.08	4.13
18	1.22	15.72	N/A	N/A	N/A	N/A
19	1.25	15.96	N/A	N/A	N/A	N/A
20	1.24	15.74	N/A	N/A	N/A	N/A
21	1.19	14.81	1.25	0.98	4.14	3.53
22	1.12	13.37	1.44	1.10	5.08	4.13
24	1.17	14.25	1.56	1.12	5.61	4.17
25	1.17	13.76	1.12	0.97	2.42	2.23
26	1.11	12.48	1.12	0.97	3.24	2.74
27	1.16	13.33	1.14	0.90	3.85	3.26
30	1.23	15.16	1.14	1.05	4.06	3.70

where $Z = \exp(Y)$ and the residuals are independent and normally distributed with mean 0 and standard deviation s_Y. For $N = 53$ measurements, s_Y is estimated as:

$$s_Y = \sqrt{\frac{\sum_{i=1}^{N} r_i^2}{N-2}}. \tag{C.3}$$

A 95.4% confidence interval for K_{Ic}^{sto} are given by the upper and lower bounds:

$$\begin{aligned} K_{Ic}^{upper} &= A\rho_{ash}^{B} \cdot exp(+2s_Y), \\ K_{Ic}^{lower} &= A\rho_{ash}^{B} \cdot exp(-2s_Y). \end{aligned} \tag{C.4}$$

The median of the log-normal error term ($Z = \exp(0) = 1$) corresponds to the deterministic correlation $K_{Ic} = A\rho_{ash}^{B}$.

References

ASTM-E1820: Standard test method for measurement of fracture toughness. Technical Report. ASTM International, West Conshohocken (2011)

ASTM-E399: Standard test method for linear-elastic plane-strain fracture toughness of metallic materials. Technical Report. ASTM International, West Conshohocken (1990)

Carpinteri A, Berto F, Fortese G, Ronchei C, Scorza D, Vantadori S (2017) Modified two-parameter fracture model for bone. Engrg. Frac. Mech. 174:44–53

Granke M, Makowski AJ, Uppuganti S, Does MD, Nyman JS (2015) Identifying novel clinical surrogates to assess human bone fracture toughness. J. Bone Mineral Res. 30:1290–1300

Granke M, Makowski AJ, Uppuganti S, Nyman JS (2016) Prevalent role of porosity and osteonal area over mineralization heterogeneity in the fracture toughness of human cortical bone. J. Biomech. 49:2748–2755

Hug L, Dahan G, Kollmannsberger S, Rank E, Yosibash Z (2022) Predicting fracture in the proximal humerus using phase field models. Jour. Mech. Behav. Biomed. Mat. 134:105415

Juszczyk MM, Cristofolini L, Viceconti M (2011) The human proximal femur behaves linearly elastic up to failure under physiological loading conditions. J. Biomech. 44:2259–2266

Katsamenis OL, Jenkins T, Thurner PJ (2015) Toughness and damage susceptibility in human cortical bone is proportional to mechanical inhomogeneity at the osteonal-level. Bone 76:158–168

Keller TS (1994) Predicting the compressive mechanical behavior of bone. J. Biomech. 27:1159–1168

Keyak J, Falkinstein Y (2003) Comparison of in situ and in vitro CT scan-based finite element model predictions of proximal femoral fracture load. Med. Eng. Phys. 25:781–787

Koester K, Ager J, Ritchie R (2008) The true toughness of human cortical bone measured with realistically short cracks. Nat. Mater. 7:672–677

Koester K, Barth HD, Ritchie R (2011) Effect of aging on the transverse toughness of human cortical bone: evaluation by R-curves. Jour. Mech. Behav. Biomed. Mat. 4:1504–1513

Langtangen HP, Logg A (2017) Solving PDEs in python: the FEniCS tutorial I. Springer, Berlin

Levy M, Vicentini F, Yosibash Z (2024) Crack nucleation in heterogeneous bars: h- and p-FEM of a phase field model. Comp. Mech. 74:661–681

Libonati F, Vergani L (2016) Understanding the structure-property relationship in cortical bone to design a biomimetic composite. Comp. Struct. 139:188–198

Nalla RK, Stölken JS, Kinney JH, Ritchie RO (2005) Fracture in human cortical bone: local fracture criteria and toughening mechanisms. J. Biomech. 38:1517–1525

Norman T, Vashishth D, Burr D (1995) Fracture toughness of human bone under tension. J. Biomech. 28:309–320

Preve D, Lenarda P, Bianchi D, Gizzi A (2024) Phase field modelling and simulation of damage occurring in human vertebra after screws fixation procedure. Comp. Mech. 74:683–702

RILEM-TC-089-FMT: Determination of fracture parameters (K_{Ic}^{S} and $CTOD_c$) of plain concrete using three-point bend tests. Technical Report. RILEM. Paris (1991)

Ritchie RO, Kinney JH, Kruzic JJ, Nalla RK (2005) A fracture mechanics and mechanistic approach to the failure of cortical bone. Fat. Fract. Eng. Mat. Struc. 28:345–371

Ritchie RO, Buehler MJ, Hansma P (2009) Plasticity and toughness in bone. Phys. Today 62:41–47

Schileo E, Dall'Ara E, Taddei F, Malandrino A, Schotkamp T, Baleani M, Viceconti M (2008) An accurate estimation of bone density improves the accuracy of subject-specific finite element models. J. Biomech. 41:2483–2491

Schileo E, Taddei F, Cristofolini L, Viceconti M (2008) Subject-specific finite element models implementing a maximum principal strain criterion are able to estimate failure risk and fracture location on human femurs tested in vitro. J. Biomech. 41:356–367

Shen R, Waisman H, Yosibash Z, Dahan G (2019) A novel phase field method for modeling the fracture of long bones. Int. J. Num. Meth. Biomed. Eng. 35:1–23

Shim J, Iwaya C, Ambrose CG, Suzuki A, Iwata J (2022) Micro-computed tomography assessment of bone structure in aging mice. Sci. Rep. 12:8117

Shin M, Zhang M, vom Scheidt A, Pelletier MH, Walsh WR, Martens PJ, Kruzic JJ, Busse B, Gludovatz B (2022) Impact of test environment on the fracture resistance of cortical bone. Jour. Mech. Behavior Biomed. Mat. 129:105155

Tanné E, Li T, Bourdin B, Marigo JJ, Maurini C (2018) Crack nucleation in variational phase-field models of brittle fracture. J. Mech. Phys. Solids 110:80–99

Trabelsi N, Yosibash Z, Wutte C, Augat R, Eberle S (2011) Patient-specific finite element analysis of the human femur—a double-blinded biomechanical validation. J. Biomech. 44:1666–1672

Wang X, Shen X, Li X, Agrawal CM (2002) Age-related changes in the collagen network and toughness of bone. Bone 31:1–7

Wille H, Rank E, Yosibash Z (2012) Prediction of the mechanical response of the femur with uncertain elastic properties. J. Biomech. 45:1140–1148

Yeni YN, Brown CU, Wang Z, Norman TL (1997) The influence of bone morphology on fracture toughness of the human femur and tibia. Bone 21:453–459

Yeni YN, Brown CU, Norman TL (1998) Influence of bone composition and apparent density on fracture toughness of the human femur and tibia. Bone 22:79–84

Yeni YN, Norman TL (2000) Calculation of porosity and osteonal cement line effects on the effective fracture toughness of cortical bone in longitudinal crack growth. Jour. Biomed. Mat. Res. 51:504–509

Yeni YN, Norman TL (2000) Fracture toughness of human femoral neck: effect of microstructure, composition, and age. Bone 26:499–504

Yosibash Z, Trabelsi N, Milgrom C (2007) Reliable simulations of the human proximal femur by high-order finite element analysis validated by experimental observations. J. Biomech. 40:3688–3699

Yosibash Z, Tal D, Trabelsi N (2010) Predicting the yield of the proximal femur using high-order finite-element analysis with inhomogeneous orthotropic material properties. Philos. Trans. R. Soc. A Math. Phys. Eng. Sci. 368:2707–2723

Yosibash Z, Mayo RP, Dahan G, Trabelsi N, Amir G, Milgrom C (2014) Predicting the stiffness and strength of human femurs with real metastatic tumors. Bone 69:180–190

Zimmermann EA, Launey ME, Ritchie RO (2010) The significance of crack-resistance curves to the mixed-mode fracture toughness of human cortical bone. Biomaterials 31:5297–5305

Zioupos P, Currey JD (1998) Changes in the stiffness, strength, and toughness of human cortical bone with age. Bone 22:57–66